2018

Calcic paleosols in a stratigraphic context from Quaggasfontein, Eastern Cape Province, South Africa: Correlations in the Wapadsberg Pass area and implications for Late Permian climate

Kaci B. Kus
Colby College

CALCIC PALEOSOLS IN A STRATIGRAPHIC CONTEXT FROM QUAGGASFONTEIN, EASTERN CAPE PROVINCE, SOUTH AFRICA: CORRELATIONS IN THE WAPADSBERG PASS AREA AND IMPLICATIONS FOR LATE PERMIAN CLIMATE

Kaci Kus ‘18

A Thesis

Submitted to the Faculty of the Geology Department of Colby College in Fulfillment of the Requirements for Honors in Geology

Waterville, Maine
May, 2018

CALCIC PALEOSOLS IN A STRATIGRAPHIC CONTEXT FROM QUAGGASFONTEIN, EASTERN CAPE PROVINCE, SOUTH AFRICA: CORRELATIONS IN THE WAPADSBERG PASS AREA AND IMPLICATIONS FOR LATE PERMIAN CLIMATE

The work described in this thesis was completed in collaboration with Dr. Robert Gastaldo and my advisory committee.

Kaci Kus

Certificate of Approval

Dr. Robert A. Gastaldo
Whipple-Coddington Professor
of Geology
Colby College

Dr. Walter A. Sullivan
Associate Professor of Geology
Department Chair
Colby College

Dr. Bess G. Koffman
Assistant Professor of Geology
Colby College

ABSTRACT

The Karoo Basin, South Africa, contains a reportedly continuous stratigraphic record spanning the terrestrial vertebrate extinction event equated with the Permian-Triassic boundary (PTB) in the marine record. The current hypothesis links this major loss in biodiversity and vertebrate turnover to a global change in climate towards aridification. Rapid climate change is interpreted to be reflected in continental rocks by a changeover from (1) greenish (Permian) to reddish (Triassic) mudrock, (2) a transition in the river architectures from meandering to braided regimes, and (3) wetland to calcic-bearing paleosols. Here, we present geochemical results on a 1.3-meter calcic paleoVertisol interval found ~34 meters below the vertebrate-defined PTB as described by previous workers. This interval differs from contemporaneous paleosols because of the presence of abundant stage II pedogenic carbonate nodules. Previous workers hypothesized that such calcic paleosols formed during the Early Triassic after the extinction event(s). As such, their presence below the biozone boundary is surprising.

The physical properties of the paleosol interval are described both in the field and with thin sections, and geochemical trends are identified through the profile. Thin sections of the siltstone, sampled at 10-cm intervals, were described to identify primary structures, fabrics, and diagenetic features. The geochemical proxies used in this study include: molecular weathering ratios and mass balance techniques. ICP-MS elemental data on bulk-rock composition were acquired at ALS Global Laboratory. Four calcium-carbonate nodules, taken from different stratigraphic positions in the paleosol profile, were analyzed for $\delta^{13}C$ and $\delta^{18}O$ at Southern Methodist University.

The calcic paleoVertisol section—one of several identified below the vertebrate-defined boundary—contains at least two stacked-soil horizons. Geochemical data indicate probable pedogenic overprinting of each soil horizon, which collectively exhibit a possible drying trend.

Mean annual precipitation (MAP) estimates transition from 890.09 mm/yr at the base of the interval to 779.88 mm/yr at its top, supporting the interpretation of a seasonal climate. Mean annual temperature (MAT) estimates remain constant at 8° C. Calcium-carbonate cemented nodules analyzed from the paleoVertisol interval have $\delta^{13}C$ values ranging from -5.44 ‰ to -8.62 ‰ and were almost certainly precipitated under well-drained conditions. The data suggest that the onset of change in paleoclimate began much earlier in the Late Permian than previously hypothesized in the Karoo Basin.

ACKNOWLEDGEMENTS

There are so many people that I would like to thank for their help in the completion of this honors thesis project. First and foremost, I would like to thank my advisor Dr. Robert Gastaldo for giving me the opportunity to do fieldwork and original research under his guidance. His patience and expertise have been invaluable throughout this writing process. I would also like to thank Dr. Walter Sullivan, Dr. Bess Koffman, and Jacob Hyatt for reading the drafts of my thesis and providing insightful comments along the way. Additionally, I would like to thank Dr. Johann Neveling and Sisanda Makubalo; the Council for Geosciences, South Africa; and Sam Sinkler from Colby College, without whom accomplishing my field work would have been impossible. Thank you to Dr. Neil Tabor for undertaking the stable isotope analyses of calcium-carbonate nodules and to Dr. Steven Driese for all of his suggestions regarding paleosol analysis. This project would not have been possible without funding from the NSF (National Science Foundation) EAR (Division of Earth Sciences) grant #1624302 to Dr. Gastaldo

TABLE OF CONTENTS

INTRODUCTION

The Karoo Basin, South Africa, is reported to hold the most complete record of sedimentation across the terrestrial Permian-Triassic Mass Extinction (PTME; Smith, 1995), which was the most catastrophic extinction event in Earth's history. The PTME is well-documented and understood in the marine realm (e.g., Payne and Clapham, 2012), where an estimated 90% of species went extinct (Erwin, 1994) between 251.941 ± 0.037 and 251.880 ± 0.031 Ma (Burgess et al., 2014). This is because the stratigraphic record in the oceans includes robust invertebrate fossil assemblages in addition to stable-isotope trends across the event (Burgess et al., 2014). Comparatively, the continental expression of the PTME is less well understood. This is because, in large part, of the difficulty that terrestrial sedimentation patterns pose for recording a continuous, unaltered record (Gastaldo and Demko, 2011). Terrestrial settings are less uniform in their depositional patterns than marine settings due to erosion, stasis, and reworking of the sediment after deposition (DiMichele and Gastaldo, 2008). This makes it difficult to conclusively determine the stratigraphic position of the PTME solely on the basis of sedimentary succession, as there is the possibility for significant variation laterally in a single locality (Gastaldo et al., 2018).

It is reported that over 70% of terrestrial vertebrates went extinct (Erwin, 1994; Ward et al., 2000; Smith and Ward, 2001) simultaneously with the marine event. One commonly invoked cause of the coeval extinction is the eruption of the Siberian Traps (Siberia, Russia), which is a large igneous province of flood basalt that began erupting ~250 Ma (Reichow et al., 2009). Their emplacement over 100,000 km^2 in a period of less than 2 Ma (Reichow et al., 2009) would have released high amounts of volcanic SO_2, CO_2, and CH_4 (Maruoka et al., 2002; MacLeod et al., 2017). Increased atmospheric greenhouse gas concentrations would have induced greenhouse warming which, in turn, may have warmed the oceans and promoted anoxia by lowering seawater

O_2 saturation levels (Macleod et al., 2017). On land, warming, aridification, acid rain, shifting climatic belts, and a reduction of atmospheric oxygen concentrations could have resulted in enhanced weathering, changes in fluvial regimes, and widespread wildfires (Macleod et al., 2017). The reduction of atmospheric oxygen may have been a result of reduced marine biodiversity as a consequence of the eruptions. Other suggested causes include bolide impact (asteroid or comet; Becker et al., 2001), ocean anoxia (Wignall and Twitchett, 1996), and oceanic overturn (Knoll et al., 1996). Conclusive evidence for any of these hypothesized mechanisms has not yet been found, and the primary cause of this extinction on land is still being debated (Retallack et al., 2003; De Kock and Kirschvink, 2004; Smith and Botha-Brink, 2014; Pace et al., 2009; Gastaldo et al., 2014; MacLeod et al., 2017).

The current terrestrial extinction model (Smith and Botha-Brink, 2014) defines the PTME on land as the last appearance datum (LAD) of the vertebrate *Daptocephalus lacerticeps* (a member of the *Daptocephalus* Assemblage Zone; Viglietti et al., 2016) and the expansion of the *Lystrosaurus* Assemblage Zone. The *Daptocephalus* Assemblage Zone previously was referred to as the *Dicynodon* Assemblage Zone (Smith, 1995; MacLeod et al., 2000; Ward et al., 2000; Smith and Ward, 2001, De Kock and Kirschvink, 2004), and a revision in the taxonomy and biostratigraphy of the assemblage zone has changed the terminology. The boundary between these biozones has been equated by many authors to the PTB (Retallack et al., 2003; Ward et al., 2005; Smith and Botha-Brink, 2014).

Smith and Botha-Brink's (2014) model for the PTME cites a shift in climate regime towards more arid conditions across the biozone boundary. This shift is accompanied by vegetational collapse as the driving force behind changes in sediment color, fluvial geomorphology, and vertebrate assemblage. The mudrocks of the Karoo are reported to change

from predominantly green in the Late Permian to red (maroon) in the Early Triassic (Ward et al. 2000, 2005). Red mudrocks have been used as evidence for a shift towards a drier, more arid climate because they are thought to represent an increased eolian contribution of iron oxide particles in arid soils (Smith and Botha, 2005; but see: Sheldon, 2005 and Gastaldo et al., 2018). Additionally, the reported change in climate resulted in a transition from a meandering to a braided river system throughout the Karoo Basin (Smith and Botha-Brink, 2014). This change in river architecture may have been the result of vegetational collapse, as proposed by Ward et al. (2000), Smith and Ward (2001), and Retallack et al. (2003), and the concomitant loss of rooted plants along riverbanks. Megafloral collapse, in turn, also led to the demise of *Daptochephalus*, a top herbivore. These changes culminate in what Smith and Ward (2001) have described as an "event bed"—a basin-wide interval of thinly-laminated red- and green-mudrock, which marks the PTB in their model.

However, there are several contradictory reports on the position of this basin-wide "event bed" (Ward et al., 2000; Smith and Ward, 2001; Retallack et al., 2003) and its relationship to the vertebrate-defined PTB. For example, Ward et al. (2000) originally placed the PTB within the event bed itself, whereas Retallack et al. (2003) placed the PTB at the top of the laminated interval, at the same localities. Smith and Botha-Brink (2014) have retained the idea that the boundary is at the top of the laminated siltsone/mudstone-couplet facies. Such discrepancies have led some researchers (Gastaldo et al., 2009, 2015) to challenge the validity of the basin-wide event bed. Basin-wide correlations, such as those involving the event bed, which rely on the physical characteristics and vertebrate biostratigraphy (Macleod et al., 2000; Smith and Ward, 2001; Retallack et al., 2003; Smith and Botha-Brink, 2014), rather than on the lateral continuity of lithological units (e.g., Gastaldo et al., 2017), must be reconsidered before further use. These ideas

only can be tested at the few localities where the vertebrate-defined boundary is reported to occur.

Wapadsberg Pass

Wapadsberg pass in the Eastern Cape Province is one of eight localities in South Africa reported to cross the critical interval that includes the vertebrate-defined PTME. The classic site is adjacent to a dirt/gravel road constructed in 1945 which, currently, is used as a farm road. Old Wapadsberg Pass road was replaced with a new tar (asphalt) road, the R61, in the latter part of the 20th century. At the present time, the site is owned by Peter Locke and is located on the farm Quaggasfontein. Exposure is found both on this farm and an adjacent farm, Piersnaarbaken.

The stratigraphy logged across Quaggasfontein and Piersnaarbaken farms in the current study (Fig. 1) differs from that previously reported in the Wapadsberg Pass area (Prevec et al., 2010; Gastaldo et al., 2014). This is due to the presence of multiple stacked, calcic paleoVertisols containing carbonate-cemented nodules (~23.5 to 25.4 m in the section, Fig. 2). Calcic paleoVertisols typically form under well-drained soil conditions (Driese et al., 2005), and, according to Smith and Botha-Brink's (2014) model, they should have formed in response to the extinction-causing aridification event(s) recorded by Early Triassic deposits. Here, however, they appear to be located in definitely Permian-age strata. Smith and Botha-Brink (2014) also report the collection of a *Dicynodon* lower jaw bone at the base of this stratigraphic section that lies 52 m below their vertebrate-defined PTB.

The goal of this thesis is to present context and geochemical data of the first reported occurrence of calcic paleoVertisols found stratigraphically below the PTB in the upper Beaufort group of the Karoo Basin. Although these data will not help constrain the current placement of the vertebrate-defined PTB in the Wapadsberg Pass area, the geochemical weathering trends of the paleosols presented here will provide insight into the climatic regime under which they formed in

the latest Permian (Changhsingian; Prevec et al., 2010).

BACKGROUND

Geologic Setting

The rocks of the study area are a part of the Karoo Supergroup (Fig. 3), which ranges in age from Late Carboniferous to Middle Jurassic (Smith et al., 1993; Johnson et al., 2006). The Karoo Basin became an ideal landlocked depositional site for continental sediment accumulation when the oceanic palaeo-Pacific plate began subducting beneath the Gondwanan plate (Smith et al., 1993). Ultimately subduction resulted the formation of the Cape Fold Belt along the southern margin of the Karoo basin. During the late Paleozoic, the Gondwanan plate also was moving southward, which was accompanied by the formation of one or more ice sheets that covered the southern portion of the supercontinent and parts of the basin. It wasn't until the southwestern half of the supercontinent Gondwana began drifting northward in the Permo-Carboniferous (~300 Ma; Smith et al., 1993) and the Early Permian ice sheet started to recede that deposition of the Karoo Supergroup was initiated. Infilling lasted over a period of ~100 million years (Smith et al., 1993).

Sediments derived from the deglaciation are placed into the first two groups deposited above Pre-Cambrian basement rock. These are the Dwyka and Ecca groups, which represent post-glacial deltaic and turbidite deposits, respectively. They are overlain by the Beaufort Group, which contains a sedimentary succession formed once the Karoo Basin was landlocked; this succession is dominated by aggradational floodplain deposits (Smith et al., 1993). There are five formations recognized in the Beaufort Group, only two of which are relevant to this project. These are the Balfour and Katberg formations (Fig. 3). The upper member of the Balfour Formation, the Palingkloof Member, is reported to span the vertebrate-defined Permian-Triassic Boundary (PTB), and the overlying Katberg Formation is considered to be Early Triassic in age (Smith and Botha-

Brink, 2014; Fig. 2).

FACTORS INFLUENCING CORRELATION IN THE KAROO BASIN

There are two major problems that present themselves when attempting to correlate localities in the Karoo based on lithology. The first problem is the reality that Karoo rocks are either very fine-grained sandstone or fine- to coarse-grained siltstone, with very little color variation (siltstone in this report will be referred to simply as either green or red in color; see Li et al., 2017 for a discussion on color). Hence, physical characteristics, alone, are not suitable for correlating widely-spaced localities. A second major problem is the fact that many Jurassic dolerite intrusions altered stratigraphic relationships throughout the basin. This means that even stratigraphic sections within a few hundred meters of each other may not represent the same interval in time due to local deformation. Because of these factors it is difficult to accurately correlate over distances greater than a few kilometers without a marker bed that can be followed for the entire correlative distance between sections.

The very limited, yet visually distinct, range of mudrock color in the Karoo Basin has not only makes correlation difficult but also has been the root of many assumptions about paleosols and the climatic regimes under which they formed. Previously, green mudrocks have been equated to paleosols that formed under wetter Permian conditions (Retallack et al., 2003; Gastaldo et al., 2014). In contrast, red mudrocks have been equated to paleosols formed under drier Triassic conditions (Ward et al., 2000; Smith and Botha-Brink, 2014; but see Sheldon, 2005). The reddening is thought to be a function of increased eolian input of hematite (Smith and Botha-Brink, 2014) in response to a more arid climate in the Late Permian and Early Triassic. However, a recent study by Li et al. (2017) on the geochemistry of red-and-green mudrocks in close stratigraphic proximity demonstrates that there are no statistically significant differences in major-element

concentrations between them. The color difference is, instead, a function of the presence of fine (<1 wt. %) early diagenetic hematite coating clay-sized grains in the red mudrocks (Li et al., 2017). Therefore, mudrock color should not be used as a diagnostic characteristic of climate at the time of deposition, as is the suggestion of Sheldon (2005).

Karoo Paleosols

Paleosols are lithified ancient soils—red and green in color in the Beaufort and Katberg formations—that formed on the floodplains adjacent to rivers. Smith (1990) identified three types of paleosol profiles as representative of the range of Late Permian soil types found in the southwestern Karoo Basin. These are interpreted to represent levee/channel-bank, proximal floodbasin, and distal floodbasin paleosols. The levee/channel-bank deposits reflect relatively immature soils (Protosols) which are recognized by their greenish color and the occasional presence of vertical calcareous tubules, rhizoconcretions, and small (<10 cm diameter), isolated calcareous nodules (Smith, 1990). The proximal floodbasin paleosols are interpreted as having accumulated off the meanderbelt slope (Smith, 1990) and are typically more reddish-brown (maroon) in color. Slickenslides and calcareous glaebules are reportedly common features. Lastly, the distal floodbasin paleosols, which are the most common paleosols, are reported to range in color from dark brown to green (Smith, 1990). Calcareous nodules are less common, although there are occurrences of small septarian nodules and "rosettes" of quartz pseudomorphs after gypsum (Smith, 1990). These three paleosols types are replaced by a single Triassic type (Smith, 1995; Gastaldo et al., 2014) that is described as primarily reddish-gray with some green mottling around rhizoconcretions (mineral cementation around fossilized roots). Horizons of well-developed calcite nodules and sand-filled desiccation cracks may also be present (Smith, 1995).

Calcic paleoVertisols

PaleoVertisols are defined as paleosols with a prominent feature of soil homogenization by pedoturbation; the dominant process by which homogenization occurs is shrinkage and swelling of expandable clay minerals (Mack et al., 1993). By definition, field recognition of this soil type requires the presence of one or more of the following morphological features: (1) dessication cracks that may be up to decimeters long, (2) wedge-shaped peds, (3) hummock and swale structure, (4) slickenslides, and (5) clastic dikes (Mack et al., 1993). The presence of expandable clays is not diagnostic, in and of itself, of a paleoVertisol because expandable clays often convert to other clay minerals during early diagenesis (smectite conversion to illite) and may not be present when analyzed. However, the presence of the expandable clay minerals strengthens an interpretation of a paleoVertisol. Calcic paleoVertisols are those that contain one or more prominent calcic horizons, regardless of the morphologic stage of the calcic nodules as defined by Machette (1985). Vertisols make up only about 2% of the world's modern soils; however, their high cohesion and bulk density (due to their high clay mineral content) may allow them to be preferentially preserved in the stratigraphic record (Driese et al., 2000).

Although comparisons between modern and ancient paleosols are not perfect, mass-balance reconstructions suggest that many pedochemical patterns are preserved in paleoVertisols (Driese et al., 2000). Studies also have shown that modern calcic Vertisols form where annual evapotranspiration exceeds precipitation (Driese et al., 2005). However, this does not necessarily imply extremely arid conditions. In a study of ancient and modern Vertisols by Nordt et al. (2006), the authors showed that annual precipitation in regions where Vertisols form could be as great as 1400 mm/year.

PREVIOUS WORK AT WAPADSBERG PASS

Ward et al. (2000) documented seven stratigraphic sections transitioning the vertebrate-

defined PTB across the Karoo Basin, one of which is at Wapadsberg Pass, Eastern Cape Province (Fig. 1). They identified three distinct facies associations. Sandstone bodies interbedded with olive-gray mudstone below the boundary show an association of sedimentary facies that are consistent with formation in large meandering rivers of high sinuosity. Their second facies assemblage is comprised of laminated sandstone-shale units, several meters in thickness, that they associated with the boundary itself. Smith and Ward (2001) termed this interval an "event bed". The third facies association is found post-boundary, and is characterized by sandstone facies typically associated with braided river systems. This third facies contains a higher proportion of sandstone to shale than in the pre-boundary facies associations (Ward et al., 2000). All three facies associations are reported to outcrop at Old Wapadsberg Pass (S31°, 54.879'; W24°, 53.794', WGS84 datum). A number of subsequent papers have detailed these sections and found discrepancies between what is reported in the literature and what appears in the physical outcrop (Gastaldo et al., 2005, 2014; Prevec et al., 2010).

A study on plant taphonomy of macrofloral assemblages reported that the trend in fossil-plant assemblages parallels the change in reported fluvial style (Gastaldo et al., 2005). At Wapadsberg Pass, only poorly preserved stem-and-leaf debris was found restricted to lateral-accretion barforms in channel deposits. At that time, poorly preserved *Glossopteris* leaves were only found beneath the event bed immediately below Smith and Ward's (2001) boundary. Subsequently, Prevec et al. (2010) recovered a plant-fossil assemblage ~70 m below the biozone boundary preserved above a weakly developed paleosol outcropping at both Old Wapadsberg Pass and a lithostratigraphically equivalent locality 1 km to the southeast at New Wapadsberg Pass. This allowed for the two localities to be correlated, and the presence of pollen allowed for an assignment to palynozones in eastern and western Australia. They assigned a Changhsingian age

to the fossil assemblage (Prevec et al., 2010).

Few comprehensive geochemical studies of the trends that encompass both pre- and/or post-boundary rocks exist from Wapadsberg Pass. Coney et al. (2007) examined the geochemical and mineralogical trends across the PTB at two localities in the Eastern Cape Province, one of which was Wapadsberg Pass (S31°, 52.474'; W24°, 54.882'). They found that changes across the PTB at this site include an increase in the elemental concentrations of all chalcophile, siderophile, and some lithophile elements; but REE abundance patterns do not vary across the boundary (Coney et al., 2007). Most recently, Gastaldo et al. (2014) published a study documenting the geochemistry of two paleosols situated ~70 m below the vertebrate-defined PTB. They found that the paleosols were indicative of wetland paleoProtosols that formed under warm-and-wet climate conditions and coincident with autochthonous *Glossopteris* forest litters (Prevec et al., 2010). They also reported stable isotope $\delta^{18}O$ and $\delta^{13}C$ values from carbonate nodules collected from a 90-m stratigraphic interval transitioning the PTB and found that there was no trend in $\delta^{18}O$. The trend in $\delta^{13}C$ demonstrated a wet-to-dry climate shift low in the section but was not indicative of aridification at the vertebrate-defined PTB. Most nodules from this section formed in saturated soils or sediments and did not record evidence of atmospheric CO_2 contribution (Gastaldo et al., 2014).

LOCALITY AND GENERALIZED STRATIGRAPHY

Quaggasfontein and Piersnaarbaken farms lie approximately 1.25 km northwest of Old Wapadsberg Pass (Ward et al., 2000; Gastaldo et al., 2005; Prevec et al., 2010). Here, a 70-m section, beginning at 24°53'19.65"E, 31°54'34.18"S and ending at 24°53'52.82"E, 31°54'35.96"S, is exposed in an erosional gully (donga; Fig. 4). A detailed stratigraphic section of this donga has not been reported before, although it is thought to transition the vertebrate-defined boundary. This

assumption is based on the report of a *Dicynodon* lower jaw bone near the base of this section (24°53'22.1", 31°54'33.4"S; Fig. 2) by Smith and Botha-Brink (2014, see their Supplementary Table 1). That fossil lies 52 m below their vertebrate-defined PTB at this locality.

The stratigraphic section of the donga that we traversed is a part of the upper Beaufort Group (Palingkloof Member of the Balfour Formation; Fig. 3). The lithologies beneath the stratigraphic position of ~57.5 m in the section have been placed into the upper *Daptocephalus* Assemblage Zone based on previously published biostratigraphy, and the overlying rocks assigned to the *Lystrosaurus* Assemblage Zone. The primary rock types found in the upper Beaufort Group are coarse- and fine-grained greenish-gray siltstones. Calcite-cemented nodules of stage I and II morphological development (Machette, 1985) are often present in the green siltstone intervals at this locality. These siltstones are occasionally interbedded with thin, low-angle crossbedded sandstone bodies.

METHODOLOGY

Lithologic logs were measured using a Jacobs staff, with Abney level, and rocks were described using standard field methods. Lithologies are characterized based on grain size, Munsell color, primary sedimentary structures, and fossil content (if present). Measurements of lithologic intervals were made to centimeter accuracy, where possible. The 1.3-m interval containing the calcic paleosols was sampled at 10-cm intervals, and hand samples were marked for thin section orientation by Dr. Robert A. Gastaldo. A brief lithologic description accompanies each sample. Samples are labeled 280517.1 to 280517.14 with 280517.1 collected from the top of the interval and 280517.14 collected from the base of the interval (Fig. 5, Table. 1). The fourteen paleosol samples were cut to standard thin-section slide size and were sent to Applied Petrographic Services in Greensburg, PA, from which thin sections were made. Samples 280517.2, 280517.3, and

280517.9 were not returned as thin sections because there was insufficient competent material. Paleosol thin sections were photographed and characterized using a petrographic microscope to identify primary structures and other unique features (e.g., cubic pyrite crystals, mud chips/clasts, and macerated plant material). Gastaldo also collected several calcite nodules from various stratigraphic heights, which were sent to Dr. Neil Tabor's laboratory at Southern Methodist University for stable carbon-and-oxygen isotope analysis (see Gastaldo et al., 2014 for methodologies). Grain size analysis (Appendix 1) and major element composition data (Appendices 2-4)—measured at Colby College using the Bruker M4 Tornado—are presented in their respective appendices.

Geochemistry

Fourteen bulk-rock and eleven thin-section samples from the calcic paleoVertisol interval were powdered using a ball mill and sent to ALS Global for a full-digestion analysis. There, samples underwent lithium borate fusion to homogenize the samples prior to acid dissolution. Inductively coupled plasma mass spectrometry (ICP-MS) analysis was used to obtain selected major and minor elemental composition data (Table 1).

Graphs for molecular weathering ratios such as base loss, clayeyness, mineral assemblage stability (MAS), calcification, salinization, and the chemical index of alteration minus potassium (CIA-K) were plotted versus profile depth following Sheldon and Tabor's (2009) parameters. To calculate the ratios, the wt% of all major elements on an oxide basis was converted to molar abundance, and the molar values were used for all of the molecular weathering ratio calculations and graphs. Base loss (Na, Ca, K, Mg/Ti) refers to the leaching of major "base" elements (Na, Ca, K, and Mg) relative to an immobile soil element (Ti) during weathering at normal pH conditions. Clayeyness (Al/Si) measures the amount of Al accumulated as clay minerals form in a soil profile.

Mineral assemblage stability (Fe/K; MAS) is a way to measure the breakdown of base-bearing minerals by hydrolysis (e.g., potassium feldspar weathering to illite). Calcification ([Ca+Mg]/Al) and salinization ([K+Na]/Al) measure the accumulation of calcium and salts, respectively, in a soil profile. CIA-K was calculated using Eqs. (1; Excel template for CIA-K calculations supplied by Dr. Neil Tabor, Southern Methodist University).

$$\text{CIA-K} = 100 \text{ x } \frac{Al}{(Al+Ca+Na)} \quad (1)$$

Bulk-rock geochemical data also were evaluated using a mass-balance approach, following Brimhall et al. (1988, 1991a,b). This approach evaluates chemical variations in a soil due to: (1) the closed-system effects of residual enrichment and volumetric changes in the soil matrix, and (2) open-system transport of material in-or-out of the soil (Driese et al., 2000). Mass-balance relationships account for changes in parent material (protolith) as a result of pedogenesis. Typically, a sample of the C-horizon is collected and used as representative parent material.

All mass balance calculations were made using a template and Eqs. (2 and 3) provided by Dr. Steven Driese, Baylor University, Texas:

$$\epsilon_{i,w} = \frac{\rho_p C_{i,p}}{\rho_w C_{i,w}} - 1 \quad (2)$$

where $\epsilon_{i,w}$ is the strain (volumetric change) of the weathered material; i is an immobile index element in the weathered material (w); ρ_p and ρ_w are the bulk densities of the parent and weathered material, respectively; and $C_{i,p}$ and $C_{i,w}$ are the concentrations of immobile element i (wt%), in the parent and weathered material, respectively. Strain ($\epsilon_{i,w}$) is used to calculated the mass fraction of

a chemical constituent that has been gained or lost in open-system transport. Mass transport ($\tau_{j,w}$) of a constituent, j, in the weathered material is measured by:

$$\tau_{j,w} = \left(\frac{\rho_w C_{j,w}}{\rho_p C_{j,p}}\right)\left(\epsilon_{i,w} + 1\right) - 1 \quad (3)$$

where all terms are described previously (Driese et al., 2000).

C-horizons were identified at depths of 30 cm and 110 cm to 120 cm based on primary sedimentary structures seen in thin section and are interpreted to be the most representative examples of parent material available from the paleoVertisol interval. Therefore, mass balance calculations for samples from a depth of 0 cm to 30 cm use the geochemical data recorded at a depth of 30 cm as representative parent material composition, and samples from a depth of 40 cm to 120 cm use an average of the geochemical data recorded at depths of 110 cm and 120 cm as representative parent material composition.

Mass balance calculations were performed to create a set of graphs representing the translocation of elements relative to the possible C-horizons identified in the calcic paleoVertisol interval. Mass balance analyses for carbonate leaching, redoximorphy, biocycling, and clay accumulation were plotted versus profile depth using Excel. Calculations and graphs were made using both Ti and Zr as immobile elements. Carbonate leaching measures the enrichment or depletion of Ca and Mg down the soil profile; redoximorphy measures the enrichment or depletion of Mn and Fe down the profile; biocycling measures the enrichment or depletion of P down the profile; and clay accumulation measures the enrichment or depletion of Na, K, Al, and Si down the profile.

It is important to note that the bulk density of the paleosols is a factor in the calculation of strain (the positive or negative volumetric changes; Driese et al., 2000) and translocation of elements in the paleosol. The bulk densities of the fourteen samples down the profile were not measured, so all mass balance calculations were made under the assumption that the bulk densities of all of the samples were 2.2 g/cm^2 (Steven Driese, personal communication, November 25, 2017).

RESULTS

The paleosol interval exposed on Quaggasfontein farm is 1.3 m thick (Fig. 5, Table 2) and is located at 31°53’60"S, 24°53'24"E. At the outcrop scale, the lithologies are well-cemented fine- to coarse-grained siltstone, the color of which ranges from olive gray (5Y 6/1) to dark greenish gray (5GY 4/1; Fig. 6A). Slickensides are not present at the sampled location, but they were occasionally found in lateral exposures along the outcrop (Fig. 6B). Most calcite-cemented nodules range in diameter from less than 1 cm to 5 cm (Fig. 6C). There are also infrequent large nodules up to 20 cm in length that form concretionary horizons (Fig. 6D). Small 1-cm-diameter nodules are distributed randomly throughout the sampled interval; however, there are several horizons in which larger nodules are concentrated (Fig. 5). According to the field classification of Mack et al. (1993), the interval conforms to the description of a calcic paleoVertisol with stage II calcic nodules.

The calcic paleoVertisol interval was sub-divided in the field into Lower Calcic Paleosol (LCP) and Upper Calcic Paleosol (UCP) intervals based on observations. The presence of a large nodule horizon (nodules 15 to 20 cm in length; Fig. 6D) marks their boundary. Samples 280517.1 to 280517.6 represent the UCP, and samples 280517.7 to 280517.14 represent the LCP. This subdivision will be revised in the discussion based on the geochemical data.

Thin sections

Textural/fabric trends. --- There are a range of textures in the siltstone, ranging from intervals with well-preserved primary structures to sediment that has been homogenized. Several thin sections exhibit well-defined intervals containing primary structures, such as coarse-fine couplets (e.g., 280517.4, 280517.12, and 280517.13; Fig. 7B, Fig. 8A, and Fig. 8B, respectively). Laminations range from sub-millimeter to 4 mm in thickness and show small-scale ripples and soft-sediment deformation (mm-scale flame structures and ripples; Fig. 8A, red arrows and "R," respectively). The coarse-fine couples in thin section 280517.4 (Fig. 7B) are neither laterally uniform in thickness nor continuous, which indicates that some alteration took place after deposition. This alteration could be the result of bioturbation, soft-sediment deformation, or soil-weathering processes. A single 0.8-mm-diameter, calcium-rich soil aggregate is also present (Fig. 7B, enlargement). In thin section 280517.12 (Fig. 8A), the basal coarse-fine couplets have widths up to 1 mm, above which distinct layering is lost until the upper third of the thin section. Here, couplets are 2 mm in thickness. Thin section 280517.12 also contains 0.5-mm-wide cubic pyrite crystals (Fig. 8A, red circles) and soil aggregates (Fig. 8A, black circles). Both 280517.12 and 280517.13 contain possible sub-vertical and horizontal sub-mm-scale burrows in finer-grained layers that have been filled with coarse silt grains (Fig. 8B, see orange and blue arrows), as well as macerated plant material (Fig. 8B, green circle).

Thin sections 280517.1 (Fig. 7A), 280517.10 (Fig. 9C), 280517.11 (Fig. 9D), and 280517.14 (Fig. 8C) display homogenized fabrics. In some cases, they contain very poorly-defined primary structures of coarse-fine couplets at the mm-scale. These thin sections are predominantly fine silt with rounded mud chips up to 2 mm in diameter. All of these thin sections also contain fragments of macerated plant material in various forms (e.g. Fig. 7A, enlargement, and Fig. 8C, enlargement).

The last fabric type—seen in 280517.5 (Fig. 7C), 280517.6 (Fig. 7D), and 280517.7 (Fig. 9A)—is composed of predominantly fine silt grains without distinct bedding. Thin section 280517.5 has abundant 2-mm-diameter, rounded mud chips scattered throughout the slide (Fig. 7C, red circles). In 280517.6, the mud chips are still present but are more elongated and more angular in morphology than in 280517.5. Finally, fractured peds and soil aggregates comprise the majority of slide 280517.7 (Fig. 9A). These aggregates can be up to 5 mm in diameter and are amorphous in shape. They are a darker brown color in PPL than the surrounding silt grains and resemble those seen in slides 280517.4 (Fig. 7B, enlargement) and 280517.12 (Fig. 8A, black circles), appearing to be amalgamations of smaller brown peds. Between the fractured peds are what appear to be sub-horizontal burrows (up to 3 mm in diameter) that are filled with coarse silt grains (Fig. 9A, orange circle).

All slides contain abundant microscopic pyrite crystals; however, larger cubic pyrite crystals, up to 0.5 mm in diameter, are visible in thin sections 280517.5 (Fig. 7C, red circle), 280517.10 (Fig. 9C, red circles), and 280517.12 (Fig. 8A, red circles). Each slide also preserves fragments of organic matter. These range from abundant 0.1-to-0.3-mm black flecks in the thin section to larger parallel and radiating forms up to 5 mm long. For example, thin section 280517.8 contains a long S-shaped form with parallel lines of organic material (Fig. 9B, enlargement). Slide 280517.1, in comparison, has several dark circular areas of organic material in the center (Fig. 7A, enlargement). Thin lines radiate outwards from the concentrated organic material.

Patterns. --- There appear to be three stacked paleosol profiles in the 1.3-m profile based on the stratigraphic position of primary structures as seen in thin section. The bounding surfaces of stacked profiles are delimited by the presence of unaltered primary structures, over which there

is an interval of homogenized siltstone. Each paleosol is separated by these sets of characteristics, and contacts between paleosols occur at depths of 30 cm and 110 cm (Fig. 5).

Thin section 280517.1 (Fig. 7A) represents the top of the 1.3-m interval; the siltstone fabric is homogenous with no evidence of primary sedimentary structures (lamination or ripples). Beneath this is a gap of 20 cm because thin sections were not able to be made from highly weathered samples (e.g., 280517.2 and 280517.3). At a depth of 30 cm in the interval, thin section 280517.4 (Fig. 7B) preserves several disturbed fine-coarse couplets. The couplets are not laterally continuous across the entire slide and are surrounded by homogenized areas. The base of the uppermost soil profile occurs here. Thin sections 280517.5 to 280517.7, which lie beneath, show no signs of lamination and have an increased abundance and size of mud chips. These are underlain by an interval of similar fabric (homogenized fine-grained silt); however, the mud chips are reduced in both size and abundance in thin section 280517.8 (Fig. 9B). There is no thin section for sample 280517.9 due to its friable nature. Thin section 280517.10 (Fig. 9C) repeats the same homogenized fabric as in slide 280517.1, except for the absence of 1-mm-scale rounded mud chips. Only one large 3-mm-diameter soil aggregate is visible in the upper right-hand corner. This is underlain by a homogenized fabric (thin section 280517.11) without mud chips and primary sedimentary structures. Thin sections 280517.12 and 280517.13 (Fig. 8A, B) contain very well-defined primary structures (coarse-fine couplets and burrows). These represent the base of the second soil profile. Slide 280517.14 (Fig. 8C) shows no distinct coarse-fine couplets. Three stacked intervals (the uppermost and bottommost being incomplete), therefore, are delimited at depths of 0 cm to 30 cm, 30 cm to 110 cm, and 120 cm to 130 cm in the outcrop.

Geochemistry results

Molecular Weathering Ratios. --- CIA-K ranges from a low value of 54.9 at a depth of 40 cm to a high value of 62.0 at a depth of 120 cm (Fig. 10). There are four positive excursions of increasing magnitude down the profile (Fig. 10) at depths of 10 cm, 30 cm, 80 cm, and 120 cm. Overall, there is a general trend of increasing values towards the profile base.

Base loss graphs (Fig. 11A) are a proxy for the leaching of major base elements—including Mg, Na, K, and Ca—relative to Ti. There is a slight overall decreasing trend down the profile for the ratio of Mg to Ti. Contrastingly, the amount of Na/Ti sharply decreases from the top of the profile down to a depth of 10 cm, followed by an increase to a depth of 90 cm. The graph of K/Ti shows an opposite trend to that of Na/Ti with a positive trend from 0 cm to 80 cm, after which there is a negative trend from 80 cm to 110 cm. From 110 cm to the base of the profile is another positive trend. Calcium is bound in two sites in the paleosol; calcium carbonate ($CaCO_3$) occurs both as nodule cement and in the siltstone matrix. Base loss only uses bulk-rock compositional data and not nodular compositional data. Hence, the trend reported (Fig. 11A) for Ca/Ti only shows the behavior of the element in the matrix. Ca/Ti has three positive excursions at depths of 20 cm, 40 cm, and 60 cm. The largest increase in Ca, at a depth of 40 cm, corresponds with a major negative excursion in CIA-K at the same position (Fig. 10). This positive excursion in Ca/Ti is followed by a generally negative trend to the base of the profile.

Trends in mineral maturity (Si/Al) and clayeyness (Al/Si) mirror each other down the profile (Fig. 11B, C). Mineral maturity shows a decreasing trend from the top of the profile to a depth of 80 cm, followed by an increasing trend from a depth of 80 cm to 1.1 m; the reverse trends is present in the clayeyness graph. Salinization ([K+Na]/Al) ranges in value from 0.46 to 0.54 and does not vary significantly down the profile (Fig. 11D). There is a weak positive trend from a depth of 0.1 m to 0.9 m and a negative trend from 0.9 m to 1.2 m. Mineral assemblage stability (Fe/K)

has both positive and negative trends down the profile (Fig. 11E). Negative excursions are at depths of 0 cm, 50 cm, and 90 cm; positive excursions are at depths of 20 cm, 60 cm, and 120 cm. Calcification ([Ca+Mg]/Al) has three positive excursions at depths of 20 cm, 40 cm, and 60 cm (Fig. 11F). Beginning at a depth of 70 cm, calcification maintains a steady value to a depth of 1 m. Below 1 m there is a slight shift towards more negative values; this shift remains relatively constant to the base of the profile.

Mass balance trends. --- Mass balance graphs show the relative translocation of major cations down the paleosol profile relative to both Ti and Zr, which are considered immobile elements (Driese et al., 2005). Mass balance graphs (Figs. 13-16) were created using geochemical data from C-horizons interpreted to be at depths where primary structures are preserved in the calcic paleoVertisol interval. Due to the high variability in relative enrichment/depletion of cations depending on which immobile element is used in the calculations, only the major trends—which remain mostly consistent irrespective to immobile element used—are reported below for the mass balance graphs. Although both Ti and Zr are generally considered to be immobile elements, modern Vertisol studies often preferentially chose to use Ti as the immobile element in their interpretations (Stiles et al., 2003; Driese et al., 2000). This is because, despite the relative chemical stability of Zr, mass-balance calculations using Zr have been found to be skewed due to sand and coarse silt additions to Verisols (Stiles et al., 2003). By comparison, Ti is generally preserved within the clay-rich soil profiles and is potentially better suited for mass-balance calculations of volume change and mobile element translocation during pedogeneisis (Stiles et al., 2003). For this reason, the results presented below will focus primarily on the trends exhibited in the graphs which use Ti as the immobile element.

Redoximorphy measures the translocation of Mn and Fe (Fig. 12). Mn data exhibit three positive excursions at depths of 20 cm, 40 cm, and 60 cm and overall enrichment above a depth of 70 cm in the profile; below a depth of 70 cm there is a relatively constant value. The two positive excursions in Mn—which occur at depths of 20 cm and 60 cm—appear to coincide with the large nodule horizons identified in the field (Fig. 5). The sudden shift to lower enrichment of Mn—beginning at a depth of 70 m—occurs directly below a large nodule horizon (nodules up to 20 cm in length) as identified in the field. Fe typically remains enriched relative to the parent material(s) and becomes increasingly enriched from the top of the profile down to a depth of 60 cm. From a depth of 60 cm to 1.1 m, Fe follows a slight negative trend, which is underlain by a slight positive trend down to the base of the interval.

Clay accumulation measures the translocation of Si, Al, Na, and K (Fig. 13). The translocation of Si indicates movement of detrital quartz through a soil. Here, Si stays relatively constant throughout the soil profiles, with no definite trend. Al and K exhibit the same trends down the profile, with K having an overall greater level of enrichment. From a depth of 0 cm to 80 cm, both Al and K exhibit positive trends, beneath which there is a decreasing trend in both elements to a depth of 1.1 m. Thereafter, Al and K increase towards the base of the profile. Lastly, Na exhibits a trend that mirrors the enrichment and depletion of Al and K. There is a net negative trend in Na from the top of the profile to a depth of 80 cm and a second decreasing trend from a depth of 90 cm to the base of the profile.

Carbonate leaching measures the translocation of Ca and Mg (Fig. 14). Mg accumulation remains relatively constant throughout the 1.3-m interval. However, there is a slight negative trend beginning at a depth of 40 cm and ending at a depth of 90 cm. Below 90 cm, Mg enrichment increases slightly. Ca, however, experiences greater fluctuations in abundance and reflects the

same trend as Mn from the redoximorphy plot (Fig. 12). Three positive excursions occur at depths of 20 cm, 40 cm, and 60 cm. From a depth of 70 cm to 1.3 m, Ca shows a net decrease. The accumulation of Ca from a depth of 20 cm to 70 cm is likely related to the presence of large nodular horizons directly above those depths.

Lastly, biocycling measures the translocation of P (Fig. 15). There appear to be two distinct negative trends in the accumulation of P down the profile, one from a depth of 0 cm to 30 cm and the other from a depth of 40 cm to 120 cm. Positive excursions occur at depths of 0 cm and 40 cm. Mn and Ca similarly experience greater enrichment at those depths. A slight positive trend begins at a depth of 90 cm and continues to the base of the profile.

Carbonate-Cemented Nodules

A suite of carbonate-cemented nodules—ranging between 3 to 6 cm in length—was collected from the paleoVertisol interval. Nodules collected from a depth of 0 cm to 50 cm were labeled as coming from the UCP, and nodules collected from below a depth of 60 cm in the profile were labeled as coming from the LCP. This division in the 1.3-m interval was based purely on observations made in the field, where a large nodule horizon was present (Fig. 5).

Description. --- Four nodules—two collected from the UCP and two collected from the LCP—were assessed for stable isotope geochemistry. These nodules range in shape from spherical to elliptical and are 4 to 5 cm in diameter. They are consistent in external color, which is typically light olive gray (5Y 6/1). All nodules have a sharp outer boundary with a dark greenish gray (5GY 4/1) to medium gray (N5) micrite fabric. Nodules are more well-cemented than the host rock.

The two LCP nodules contain septarian cracks (Fig. 16A, B), whereas the two UCP nodules exhibit no cracking (Fig. 17A, B). The cracks in the LCP nodules are filled with calcite spar. One of the nodules has a septarian crack in the form of a single spar ring in the center of the nodule that

surrounds a central fabric; this central fabric is slightly lighter in color than the peripheral fabric (Fig. 16A). The other septarian nodule (Fig. 16B) is more irregular in morphology. The septarian cracks in this second nodule are smaller and are not focused around the center of the nodule. The two nodules taken from the UCP do not show any signs of recrystallized calcite spar (Fig. 17A, B). Another key difference is that the septarian nodules are flecked with greenish black (5G 2/1).

Stable isotope results. --- The four nodules taken from different stratigraphic heights were analyzed for $\delta^{13}C$ and $\delta^{18}O$ and represent a pilot study. Values for $\delta^{13}C$ (‰VPDB) range from -8.62 to -5.44, and values for $\delta^{18}O$ (‰VPDB) range from -21.24 to -21.71 (Table 3). These data can be compared against Gastaldo et al.'s (2014) analyses of carbonate-cemented nodules from Wapadsberg Pass.

DISCUSSION

The recognition of paleosols in the Karoo Basin began in the late 20th Century. Smith (1990) reported three types of paleosol profiles in the Teekloof Formation (the upper half of which is correlated with the lower half of the Balfour Formation), which are based on their geographic proximity to ancient river systems. These soil types are distributed across the floodplain and are interpreted to have been coeval.

The paleosols of the levee facies are interpreted to be channel-bank successions. They consist of rapidly alternating green, grey, and rare reddish-brown siltstone and buff-and-green-colored, fine-grained sandstone beds (Smith, 1990). The siltstone beds are reported to contain abundant smooth-surfaced calcareous glaebules (a term used to encompass the range of morphologies that calcium carbonate can form in a soil; Brewer, 1964). Oblate nodules—ranging in length from a few mm to 25 cm—are concentrated in the lower horizons of these paleosols. Most nodules are in the 5- to 10-cm range, with smaller nodules tending to be more spherical; this

is in contrast with larger nodules, which tend to be both amalgamations of several smaller nodules and more irregular in shape. These paleosols also contain rhizocretions in the upper horizons.

The lateral facies equivalents of Smith's (1990) levee deposits are termed the proximal floodbasin paleosols and are interpreted to be calcic Vertisols due to the presence of slickensides. According to Smith's (1990) model, these paleosols are the equivalent of the Old Wapadsberg Pass paleosols. The mudrock colors are more variable than in levee deposits with more reddish-brown, brown, and mottled purple horizons. This facies is also reported to contain abundant calcium-carbonate cemented glaebules—usually irregular and knobbly in appearance (Smith, 1990). These are interpreted to form in response to the amalgamation of smaller nodules and occur in "clumps" up to 5 mm in diameter and 10 cm in thickness. The nodules in these paleosols tend to occur in sheet-like horizons, with solid beds of calcareous micrite between nodular horizons. Broken nodules contain claystone-lined burrows and root channels. Black cubic crystals were identified in many of the nodules, as were star-shaped cavities or arcuate fissures filled with equant calcite and manganese oxide. Smith (1990) does not identify the black cubic crystals as pyrite or the calcite-filled cavities/fissures as septaria; however, those interpretations seem applicable. Rhizocretions are not as abundant as in the levee deposits, and calcified coprolites and calcretized burrow casts are minor components of these paleosols (Smith, 1990).

The most distal paleosol is termed the distal floodbasin facies (Smith, 1990). The parent materials that formed these paleosols were deposited in the axial depressions of floodbasins far from the main rivers. They consist of thinly-bedded dark grey and dark brown shales with thin, persistent beds of green siltstone and horizontally laminated fine-grained sandstone (Smith, 1990). Calcium-carbonate nodules are not as common, although a type of paleocaliche—consisting of a polygonal network of calcareous nodular material—was rarely encountered. Sometimes, quartz

pseudomorphs after gypsum are reported to occur as "rosettes" ("desert rose") clusters (Smith, 1990).

The same three types of paleosols (Smith, 1990) that occur in the Teekloof Formation are also reported as occurring in the *Dicynodon* (Daptocephalus) Zone of the Balfour Formation to the east (Smith, 1995). In contrast, the *Lystrosaurus* Zone paleosols tend to be rubified, contain rhizocretions, and have more well-developed calcic horizons.

A subsequent study of Karoo paleosols identified distinctive Permian and Triassic soil types. Retallack et al. (2003) describe calcic horizons in paleosols both below and above the vertebrate-defined PTB (proposed to be time-equivalent to the laminated "event bed"). Below the event bed of Smith and Ward (2000), calcic horizons are diffuse and shallow. In contrast, above the event bed the calcic horizons are deep and well-focused. Paleosols below the PTB are described as purple-red (10R) and gray, and those above are described as brownish red (2.5YR) and green. Paleosol classification by Retallack et al. (2003) was made based on field observations (e.g., nodule development, clay-skin density, and color) and supplemented by limited geochemical analyses using molecular weathering ratios. Some nodules were found to contain sparry calcite, interpreted as the result of neomorphism at depth. The majority of the nodules did not contain sparry calcite and were composed of micritic pedogenic carbonate.

The calcic paleoVertisol profile of the current study has similarities and differences with previously-described calcic paleosols/paleoVertisols in the Teekloof and Balfour Formations. The presence of abundant 1-to-5-cm-diameter spherical nodules, rare accretionary horizons of 15-to-20-cm-long nodules, occasional septarian nodules, and slickensides make the calcic paleoVertisol on Quaggassfontein farm most similar to the proximal floodbasin facies of Smith (1990), with similarities also to his levee facies. The Quaggasfontein paleosols and Smith's (1990, 1995)

proximal floodplain paleosols both contain slickensides and septarian nodules. Their main difference is that, on average, the nodules reported by Smith (1990, 1995) are larger (5 to 10 cm) and often clumped together. The Quaggasfontein paleosols do not display distinct siltstone layering between thin sheets of calcareous nodules, and no rhizocretions were identified in the field. In contrast, the nodules of the levee facies (Smith, 1990) are generally more spherical and are amalgamated together less often than those of the proximal floodplain facies. No gypsum rosettes were identified at Quaggasfontein.

Cubic crystals, assumed here to be pyrite, were identified by Smith (1990) in some calcite nodules. Although we did not find cubic pyrite crystals in the Quaggasfontein nodules, sub-mm-scale cubic pyrite occurs in the siltstone surrounding the nodules (Figs. 7-9). Larger cubic pyrite crystals, up to 1 mm in length, are very abundant and concentrated on bedding contacts in some of the sandstone bodies throughout the stratigraphy at Quaggasfontein (Fig. 2). In contrast, the pyrite within the siltstone intervals tends to be smaller—often not visible without a hand lens—and more dispersed (not confined to bedding surfaces). The pyrite in the sandstone is interpreted to be intraformational because it often occurs in a sheet-like distribution on a bedding surface. Therefore, sulfur reduction is thought—because of its random distribution in siltstone—to have originated in the siltstone, where it produced the pyrite.

The genesis of the previously unreported pyrite in the Wapadsberg Pass area is still not understood. Its unexpected abundance throughout the 70-m stratigraphic interval (Fig. 2) indicates that there must have been: (1) a significant and somewhat constant source of sulfur, (2) early diagenetic conditions promoting sulfur-reducing bacterial activity, and (3) periodic anoxic conditions at this locality. Thomas et al. (2011) report sulfur is typically provided from some sort of marine source in modern soils. However, in instances where there is no evidence of a marine

incursion or a marine-sourced parent material—as is the case with the Balfour Formation—the Earth's atmosphere can provide an alternative source of sulfur (Thomas et al., 2011). Marouka et al. (2003) report elevated sulfur concentration in rocks at and just below the perceived PTB in the Karoo Basin. They determined the enhanced sulfide was most likely a result of acid rain from volcanism (Marouka et al., 2003). This explanation would be consistent with the co-occurrence of the emplacement of the Siberian Traps with the vertebrate-defined PTB (Maruoka et al., 2003) or is perhaps related to volcanic activity in the Cape Fold Belt during the Late Permian (Blewett and Phillips, 2016). Because (1) Quaggasfontein is comprised of primarily dark greenish-gray siltstone, and (2) we did not specifically look for pyrite in the rare, reddish-gray siltstone, it is yet to be determined whether cubic pyrite formation is related to siltstone coloration.

The Quaggasfontein paleosols are almost always dark greenish-gray in color and do not exhibit any color banding as described by Smith (1990) for his proximal floodplain facies. Rare brownish-gray (5YR 4/1) mudrock intervals were found low in the Quaggasfontein stratigraphic section (Fig. 2), and some brownish-gray mottling occurs adjacent to the sampled LCP. That mottling disappears laterally. Smith (1995) describes the paleosols in the *Dicynodon* (*Daptocephalus*) zone as being mainly purple-red and gray, and he describes those in the *Lystrosaurus* zone as being reddish-brown and greenish-gray. These color descriptions do not conform with paleosol coloration at Quaggasfontein, as the calcic paleoVertisol interval is in the *Dicynodon* (*Daptocephalus*) zone.

The physical and stratigraphic location of these soils does not conform to the Karoo Basin model (Retallack et al., 2003; Smith and Botha-Bring, 2014). All nodules in the calcic paleoVertisol at Quaggasfontein have well-defined boundaries. Based on Retallack et al.'s (2003) description of nodular horizons below and above their vertebrate-defined PTB, such well-defined

nodules should be located exclusively in the *Lystrosaurus* Zone. Retallack et al. (2003) report nodules with diffuse boundaries as being restricted to the *Dicynodon* (*Daptocephalus*) Zone. The observations made in this study demonstrate the presence of well-defined nodules in Late Permian strata below the vertebrate-defined PTB of Smith and Botha-Brink (2014) formed at this locality.

Descriptive shorthand for paleosol horizons

The horizons identified in this study can be placed into two master soil horizons: B, and C (Thomas et al., 2011; Table 4). The B-horizon underlies an A-horizon—which is located beneath an O-horizon (surface accumulation of organic material; Gastaldo et al., 2014) and contains a mixture of organic and mineral matter—and is enriched in some mineral material compared to both underlying and overlying horizons, or it is more weathered. The C-horizon lacks the properties of other soil horizons but show limited accumulation of silica, carbonates, and soluble salts. Often in floodplain soils, the C-horizon preserves primary sedimentary structures.

Subordinate descriptors—such as t, k, and w—can be applied to better detail the nuances within the master horizons. The letter t denotes a horizon that is rich in phyllosilicates (clays; Thomas et al., 2011). The letter k is used to describe the accumulation of carbonates (Thomas et al., 2011). The last subordinate descriptor used in this study, w, describes a colored or structural B-horizon (Thomas et al., 2011).

Identification of correlative trends

Geochemical data (CIA-K, molecular weathering ratios, and mass balance calculations) from the 1.3-m calcic paleoVertisol interval, in combination with physical properties of thin sections, exhibit a wide range of trends and depths at which positive and negative excursions occur (Fig. 18). There are several possibilities as to why a wide range exists in the data. One reason may relate to the sampling protocol used in the field—where measurements were made at 10-cm

intervals—and the incompetent nature of the siltstone, which made producing thin sections difficult. Another reason may be that different types of data are being evaluated individually for trends and are subsequently compared. For example, observations made in the field are at a much lower resolution—as these observations are limited by the weathered siltstone—than observations made of thin sections. This could explain why only two paleosol profiles were identified in the field, while the possibility of three profiles are identified based on thin section features. A reason for discrepancies in the soil depth at which excursions in the geochemical graphs occur is that different elements may be moved to, or accumulate at, different depths in a soil profile. For example, carbon—which originates from organic matter—is generally most concentrated at the tops of soils, (i.e., in the O- or A-horizons). Likewise, a mobile element—such as Na—is likely to be leached relatively rapidly and, thus, will be concentrated at greater depths in the soil profile. Therefore, even though excursions in two different molecular weathering proxies or mass balance trends may not correlate at depth, they could be representative of the same soil profile. It is evident from the geochemical graphs that certain weathering proxies and the translocation of certain elements share similar—if not identical—trends down the sampled outcrop profile. Correlative excursions that mark depths of significant change are not isolated from one another, and some graphs share trends across multiple proxies.

Molecular-ratio proxies for calcification ([Ca+Mg]/Al) and base loss (Ca/Ti), as well as mass balance graphs for Ca and Mn, all share positive excursions at depths of 20 cm, 40 cm, and 60 cm (Fig. 18). Due to the close vertical proximity of these excursions to one another, they are interpreted to represent a general interval of elevated values in the upper half of the profile. It is possible that these three positive excursions mark the tops or bottoms of additional soil horizons.

However, because our data were sampled at 10-cm intervals, it is impossible to confidently assume there are significant trends between the 20-cm intervals of the excursions.

It is not surprising that calcification, base loss, Ca, and Mn exhibit similar trends because these graphs track the behavior of elements that are very sensitive to soil-moisture content. Calcification graphs the enrichment/depletion of Ca down the soil profile; base loss graphs the ratio of Ca to Ti (an immobile element); and, similarly, Ca graphs the translocation of Ca relative to Ti and Zr. Calcium in this paleosol is found in both the matrix and the calcareous nodules. Interestingly, positive excursions of %TIC (see Appendix 9) occur at the same depths as those in graphs of Ca (Fig. 14). This could mean that both Ca and %TIC are more abundant in the matrix at these depths than at depths below 60 cm, where values of Ca and inorganic carbon in the matrix are lower. Mn is a redox-sensitive trace element, and its behavior is very dependent on the mobility of water in the soil (Driese et al, 2000). The relatively high enrichment peaks at depths of 20 cm, 40 cm, and 60 cm indicates that low moisture in the soil column did *not* result in the strong leaching of Mn. This is supported by the significant drop in enrichment of Mn below a depth of 60 cm, which could be a result of the evaporation-wicking of soil moisture and the transportation of Mn upward in the soil (Driese et al., 2000); relatedly, Stiles et al. (2003) showed that—in Quaternary-age Vertisols—Mn tended to be depleted at greater depths (and accumulated at shallower depths) when mean annual precipitation (MAP) was <1150 mm/yr. These four graphs (Fig. 11A, F, Fig. 14, and Fig. 12) indicate that the movement of Ca and Mn is likely not restricted to any one soil profile. Therefore, even though several excursions (MAS, TL P, and TL Fe; Fig. 18) can be identified coincident with excursions in calcification, base loss, Ca, and Mn, the depths at which these are found (20 cm, 40 cm, and 60 cm) do not necessarily correspond with boundaries between original soil profiles.

The next depth at which five positive (though also one negative) excursions occur is at 80 cm (Fig. 18). At this depth, base loss (K/Ti), mineral maturity (Si/Al), clayeyness (Al/Si), and the translocation of K and Al exhibit major shifts. The translocation of K and Al tracks clay accumulation (Fig. 13) as do the molecular-ratio proxies for clayeyness and mineral maturity (Sheldon and Tabor, 2009). The four graphs support the interpretation that 80 cm is a depth at which clays accumulated.

Three positive excursions (Na, base loss [Na/Ti], and salinization) and two negative excursions (Mg and MAS) occur at a depth of 90 cm (Fig. 18). All positive excursions are associated with major elements that are readily leached in soils (Stiles et al., 2003; Sheldon and Tabor, 2009). The accumulation of clays and salts is likely related to the elevated levels of clay accumulation at a depth of 80 cm. Contrastingly, Mg and MAS exhibit negative excursions at this depth. Both Ca and Mg are elements that form carbonate minerals. The significantly lower Mg values compared to Ca at a depth of 90 cm implies either that the weathered parent material provided less Mg or that more Mg may be sequestered in carbonate cements, leaving more Ca in the matrix at this depth. MAS measures the breakdown of base-bearing minerals by hydrolysis, and a negative excursion indicates that many of the original minerals have been broken down and weathered to clays (Sheldon and Tabor, 2009).

Lastly, the greatest number of coincident excursions occurs at a depth of 110 cm. Graphs for Fe, K, Al, base loss (K/Ti), and clayeyness all exhibit negative excursions at this depth, whereas mineral maturity exhibits a positive excursion. The relatively low abundances of elements are indicative of clay accumulation; leaching at a depth of 110 cm implies the presence of a soil profile boundary. Driese (2004) showed that the translocation of Fe in modern Vertisols is a function of mean annual precipitation (MAP) and soil age, with greater total Fe losses with greater MAP and

age. Ignoring the factor of age, which cannot be determined for the Quaggasfontein paleoVertisols, the relatively low enrichment of Fe at a depth of 110 cm—compared to the positive excursion at a depth of 60 cm—may be indicative of dry conditions.

Soil profile boundaries

Based on the presence of well-defined primary structures (e.g., coarse-fine couplets) in the thin sections, boundaries between soil horizons are placed at depths of 30 cm and 110 cm (primary structures were also found at a depth of 120 cm). These depths are interpreted to represent the bases of soil profiles because primary structures are typically altered through soil weathering processes and bioturbation, which occur at lower depths. Their preservation is a sign of minimal soil weathering. The following soil profiles do not take into consideration the interval from a depth of 120 cm to 130 cm because this interval has insufficient data.

Profile 1: 30 cm to 120 cm. --- The upper half of this profile is dominated by positive excursions of several proxies at depths of 40 cm and 60 cm. Positive excursions in calcification, base loss (Ca/Ti), Ca, and Mn (Fig. 18) indicate that soil moisture content was low, resulting in a poorly-leached paleosol. These elements are associated with calcareous nodule formation and may indicate that fewer nodules were formed in the upper horizon of the profile. Thus, there are higher abundances of these elements in the silt matrix. This supports the interpretation that the interval from a depth of 30 cm to 60 cm is a Bk-horizon.

There are positive excursions in K, Al, base loss (K/Ti), and clayeyness at a depth of 80 cm (Fig. 18). This depth is interpreted to represent a Btk-horizon because the high concentration of elements is indicative of clay minerals. The interval from a depth of 90 cm to 110 cm is interpreted to be a Bw-horizon because of the high values of mineral maturity (indicating original minerals have not been weathered to clays) and depletion of elements such as K and Al, which are

also associated with base loss and clayeyness (Fig. 18). The interval beginning at a depth of 110 cm and continuing to a depth of 120 cm is interpreted to be a C-horizon because of the abundant, well-defined coarse-fine couplets, which are indicative of less soil weathering.

Profile 2: 0 cm to 30 cm. --- This 30 cm interval is interpreted as representing a partial soil profile due to an absence of data above the 0 m position (a few cm above which lies an erosional contact with a sandstone body). There are negative excursions in base loss (Na/Ti) and salinization, which are interpreted as being signs of low moisture during soil formation; this is because low salinization values near the base of a soil are interpreted to represent insufficient soil moisture that allowed for the translocation of salts down the soil column. Similar to the fourth soil profile of the TOC-defined profiles, this uppermost interval is interpreted as being a Bk-horizon (Fig. 18).

Five positive excursions in soil proxies occur at a depth of 20 cm. These include MAS, Mn, Ca, base loss (Ca/Ti), calcification, and %TOC. High values of MAS are indicative of minimal weathering of original minerals (Sheldon and Tabor, 2009); however, the accumulation of Mn and Ca, and the values for base loss and calcification directly above the interpreted base, indicate sufficient moisture to leach these elements down the solum. Therefore, the high MAS value is somewhat contradictory to the high accumulation of major elements at this depth. One possible explanation for this phenomenon may be that the accumulation of Mn and Ca and the values for base loss and calcification are related to the elevated levels in those same proxies at depths of 40 cm and 60 cm. This ~40 cm zone is indicative of an overprinted signature of elevated values in response to polygenetic soil forming processes. The positive excursion in MAS is, therefore, interpreted to be more representative of the original signature of this soil than the other excursions.

Climate Implications

According to Sheldon and Tabor (2009), mean annual precipitation (MAP) and mean annual temperature (MAT) can be calculated using molar ratios of CIA-K (Eqs. 1) and salinization, respectively, from paleosol geochemical data (Table 5). MAP is related to CIA-K and is calibrated for precipitation values between 200 and 1600 mm/year using the equation:

$$\text{MAP (mm/year)} = 221e^{0.0197(\text{CIA-K})}, \quad (4)$$

where the CIA-K = 100 x $[Al_2O_3/(Al_2O_3 + CaO + Na_2O)]$ with an error of ±181 mm/year. The CIA-K value of the Bt horizon is used to calculate MAP (Sheldon and Tabor, 2009). A high CIA-K value is indicative of a high degree of weathering; even if no well-developed Bt horizon was identified for a soil profile (e.g., soil profile 1; Fig. 18), the positive excursions in CIA-K are used. Sheldon et al. (2002) also state that the relationship between CIA-K and MAP is not useful for desert soils, waterlogged soils, disturbed soils, or soils forming on significant topographic relief. However, these constraints should not pose a problem because the Quaggasfontein paleosol(s) are not suspected of having formed under any of these conditions. The CIA-K values at depths of 10 cm and 80 cm—corresponding with the first and second soil profiles, respectively—are used in the MAP calculations. Although the CIA-K values at these depths are not necessarily the maximum excursions seen in CIA-K (Fig. 10), these depths correspond with estimated Bt-horizons based on the integration of the other geochemical proxies. MAT is calculated with the equation:

$$\text{T(° C)} = -18.5\,S + 17.3, \quad (5)$$

where S is the salinization ([K+Na]/Al) value of the Bt horizon and standard error is ±4.4° C with an R^2=0.37 for the empirical fit (Sheldon and Tabor, 2009). For consistency, the same depths that

were used as Bt horizons—based on the CIA-K values—are used for salinization values in the MAT calculations.

The MAP of soil profile 1 is calculated to have been 890.09 ± 181 mm/year, with a MAT of 8.35 ± 4.4° C (Table 5). The MAP and MAT of the overlying soil profile (soil profile 2) should be regarded cautiously because it is almost certainly an incomplete record, and it is unknown how the chemostratigraphy may change above a depth of 0 cm. The MAP of the second soil profile is calculated to have been 779.88 ± 181 mm/yr, and the MAT is 8.67 ± 4.4° C (Table 5).

Based on the interpretation that primary sedimentary structures are representative of the bases of soil profiles, there are no apparent trends in MAP or MAT between the first and second soil profile. Both of the changes in MAP and MAT calculated using Sheldon and Tabor's (2009) paleoprecipitation and paleotemperature (applicable to lowland settings) equations are within the standard errors of their respective equations. The change in MAP is -110.21 mm/yr, and there is only a +0.32° C difference between soil profile 1 and soil profile 2.

Implications for vertebrate-defined PTB

Based on the collection and identification of a *Dicynodon* lower jaw bone from a stratigraphic height of ~5.5 m in the measured section (Fig. 2), Smith and Botha-Brink (2014) placed their vertebrate-defined PTB in the Wapadsberg Pass area at 52 m above the *Dicynodon* bone. This places their boundary on Quaggasfontein farm at a height of ~57.5 m in the stratigraphic section (Fig. 2). The calcic paleoVertisol interval—which occurs from a stratigraphic height of ~23.5 to 25.4 m—is, therefore, situated below Smith and Botha-Brink's (2014) PTB in the *Dicynodon* (*Daptocephalus*) Assemblage Zone. Additionally, a well-preserved gorgonopsian tooth—a predator that went extinct before the PTB—was recovered by Kus et al. (2017) *above* the intervals of calcic paleoVertisols at a stratigraphic height of ~51 m in the section (Fig. 2). This

further confirms that these paleosols are Late Permian in age.

A previous study by Gastaldo et al. (2014) interpreted paleosols found in the Wapadsberg Pass area—located ~70 m below the vertebrate-defined PTB—as representing a highly seasonal climate that fluctuated between wet and dry periods. They documented two stacked immature wetland soils in which O-horizons are preserved, and two stratigraphic horizons where vertical roots are preserved inside carbonate-cemented nodules (Gastaldo et al., 2014). Carbonate nodules below the immature paleosols represent pedogenesis in a wet environment, whereas nodules found at the contact between laminated siltstones and overlying sandstones above the paleosols exhibited a dry seasonal signature (Gastaldo et al., 2014). This is a somewhat different geochemical and stable-isotope signature than was found at the Quaggasfontein locality.

Geochemical data from the calcic paleoVertisol profiles are possibly indicative of a trend towards more seasonally dry conditions over time. The MAP of the soil profiles decreases in the younger soil profile from 890.09 ± 181 mm/yr to 779.88 ± 181 mm/yr (Table 5). Although soil profile 2 experienced an estimated 110 mm/yr less MAP than soil profile 1, this cannot conclusively be identified as a drying trend, as the difference in MAP between the two profiles is within the standard error of the equation. Conversely, the difference in MAP of the two soil profiles could potentially be as great as 472 mm/yr depending on the error of the estimated values.

The stable-isotope data of four nodules taken from the UCP and LCP indicate that these nodules formed under almost certainly well-drained conditions. The $\delta^{13}C$ values range from -8.62 to -5.44 (Table 3). Gastaldo et al. (2014) showed that $\delta^{13}C$ values more positive than -8 are indicative of almost certainly well-drained conditions, and $\delta^{13}C$ values more negative than -12 are too negative for well-drained conditions. Hence, the nodules contained in both the upper and lower portions of this study are interpreted to have been formed under well-drained conditions.

The physical features of the paleoVertisols interval are interpreted to have formed under seasonally dry climatic conditions. Seasonality is evidenced by the presence of: (1) slickensides, (2) septarian concretions, (3) scattered stage II calcium-carbonate nodules (Mack et al., 1993), and (4) multiple generations of nodules (indicated by varying size/diameter). Previous researchers (Smith and Ward, 2001; Ward et al., 2005; Smith and Botha-Brink, 2014) have proposed that the shift in climate occurred rapidly at the end of the Permian; however, the shift in climate towards more seasonally dry conditions well below the PTB at Quaggasfontein implies that the onset of climate change may have been more gradual and begun earlier than previously hypothesized.

The interpretation of earlier onset of the PTME is supported by findings by Viglietti et al. (2018), who identified four facies associations in the Beaufort Group (*Daptocephalus* Assemblage Zone), one of which (a lacustrine/sub-aqueous system) is reportedly present only in the Lower *Daptocephalus* Zone. They indicate a loss in their facies 4—thin tabular sandstone interbedded with rhythmitic (heterolithic) fine sandstone and green shale—in the upper part of the Assemblage Zone. They interpret this to demonstrate that paleoenvironmental changes were occurring low in the Upper *Daptocephalus* Zone and below the phased extinctions of Smith and Botha-Brink (2014).

The 1.3-m section exposed on Quaggasfontein is a snapshot of an unknown length of time beneath the vertebrate-defined boundary. To gain a better understanding of how the climate continued to change approaching the biozone boundary, further studies would have to be performed on several calcic horizons identified at higher stratigraphic levels in the measured section (Fig. 2). The presence of several similar carbonate-nodule-bearing horizons above the one sampled in this study strongly suggests that this period of increased seasonality was not a unique occurrence in the Late Permian. These data—in conjunction with those of the previous study by

Gastaldo et al. (2014)—suggest that strong seasonal periodicity may have been punctuated by seasonally drier periods that affected the Wapadsberg Pass area.

CONCLUSIONS

The Karoo Basin, South Africa, has been used—since the late 20th Century—as a model for the paleoenvironmental and climatic changes that occurred across the vertebrate-defined Permian-Triassic. The widely accepted model, proposed by Smith and Botha-Brink (2014), describes a three-phased extinction event that occurred over a period of some 120,000 years and was driven primarily by rapid, progressive climatic drying and increased expression of seasonality. This model of rapid drying and extinction (Retallack et al., 2003) has not been strongly substantiated by several detailed geochemical analyses (e.g., Coney et al., 2007), with even less attention paid to paleosols as records of paleoenvironmental factors. This study is the first to examine a calcic paleoVertisol, which outcrops at Quaggasfontein farm in the Wapadsberg Pass area (paleosol interval begins at 31°53’60"S, 24°53'24"E).

In addition to recording the macro- and micro-morphological characteristics of these paleosols, several geochemical analyses were performed to understand the environmental conditions under which the paleosols formed. The 1.3-m section was sampled at 10-cm intervals, and petrographic thin sections were examined. The geochemical data collected from fourteen bulk-rock samples were used to calculate molecular-ratios and mass-balance weathering proxies. Based on the integration of the results of these analyses, it is concluded that the calcic paleoVertisol interval from Quaggasfontein represents at least two stacked soil profiles, pedogenically altered in a floodplain setting. The boundaries of the two soil profiles have been tentatively placed at depths at which primary sedimentary structures are preserved in thin section. These depths were chosen as the base of each soil, however, there are other possible interpretations that could be made (see

Appendix 9). Additionally, a possible drying trend was found across the two soil profiles; however, further data would be required to interpret more conclusively as the change in MAP is still within the standard error of the equation. The $\delta^{13}C$ data confirm that the nodules formed under almost certainly well-drained conditions. Despite the possible drying trend up the paleosol profiles, MAT remained constant around 10° C in all soil profiles. These findings agree with those reported by Knight (2010), who reports that stacked inceptisol horizons analyzed from a Wapadsberg Pass section are indicative of a highly seasonal climate during the Late Permian (MAT of 12.24 ± 4.4° C and a MAP of 1200.21 ± 181 mm/yr). The calcic paleoVertisols of this study likely formed during one or more seasonally dry periods. The stratigraphic position of the calcic paleoVertisol interval at Quaggasfontein, ~34 m below the vertebrate-defined PTB (Smith and Botha-Brink, 2014), indicates that a change in climate towards increased seasonality began well before the purported extinction event(s). These findings, in addition to those of Viglietti et al. (2018), support a hypothesis of more gradual climate change—or at least earlier onset of climate change—during the Late Permian.

Although this study presents a robust data-set from which to interpret paleoenvironmental changes across the calcic paleoVertisol interval, there are several caveats. Due to the highly weathered nature of the calcic paleoVertisol outcrop, bulk rock samples were only able to be taken at a resolution of 10-cm intervals. While this resolution provides a general idea of the trends through the 1.3-m section, it was not expected that two to four (or more) stacked profiles might be present. Each soil profile could be much better understood if additional samples were available for analysis. The mass balance calculations pose another potential source for error. No discernable C-horizon was identified in the field; however, based on the occurrence of well-preserved primary sedimentary structures in thin sections, C-horizons were interpreted to be preserved at depths of

30 cm and 110 cm to 120 cm. These depths are assumed to be representative of unweathered parent material that originated from the Cape Fold Belt. However, there is no way to guarantee that this material is indeed unaltered by pedogenic processes. Another source for possible error in the interpretations is the fact that mass-balance calculations require data on the bulk rock density of the paleosols. Because these data were not measured, a general bulk density value representative of a paleoVertisol was used for all of the samples. This could potentially affect the magnitude of enrichment and depletion trends in the mass-balance graphs. Additionally, the discussion presented here focuses on trends in the mass balance graphs that use Ti as the immobile element because the calculations made using Zr are assumed to be less representative of translocation due to pedogenic processes in a Vertisol. It is possible, however, that the calculations made using Zr are actually more representative of the actual movement of elements in this paleosol. This study presents two possible interpretations of the soil profiles based primarily on the general trends across several data sets; however, giving more weight to the values of enrichment/depletion/molecular-ratios down the profile could support other interpretations. Future studies should attempt to sample at a higher stratigraphic resolution and analyze more of the calcareous nodules for stable isotopes. The previously unreported presence of cubic pyrite crystals—which are found throughout the 70-m measured section—in both siltstone and sandstone bodies could also contain pertinent information about the possible cause of the PTME if sulfur isotope analyses were performed to determine the origin of the sulfur.

This study shows how paleosols—which are sensitive and specific to the environments in which they were formed—can be used to aid in paleoclimate and paleoenvironment interpretations. Similar detailed geochemical studies of paleosols below, at, and above the vertebrate-defined boundary would help constrain the terrestrial conditions leading up to, at, and after the largest mass

extinction in Earth's history. Although the scope of this study cannot draw conclusions about the conditions that occurred at the vertebrate-defined boundary or even where that boundary might be placed, it does provide the insight that the climate was likely experiencing seasonally dry periods much earlier in the Late Permian than has been previously hypothesized.

REFERENCES

Becker, L., Poreda, R.J., Hunt, A.G., Bunch, T.E., and Rampino, M., 2001, Impact event at the Permian-Triassic boundary: evidence from extraterrestrial noble gases in fullerines: Science, v. 291, p. 1530-1533.

Blewett, S.C.J., and Phillips, D., 2016, An Overview of Cape Fold Belt Geochronology: Implications for Sediment Provenance and the Timing of Orogenesis: *in* Linol, B., and de Wit, M., eds., Origin and Evolution of the Cape Mountains and Karoo Basin: Regional Geology Reviews, Springer Publishing, p. 49-55.

Brewer, R., 1964, Fabric and mineral analysis of soils: New York, John Wiley & Sons, Inc., p. 258-260.

Brimhall, G.H., Lewis, C.J., Ague, J.J., Dietrich, W.E., Hampel, J., Teague, T., and Rix, P., 1988, Metal enrichment in bauxites by deposition of chemically mature Aeolian dust: Nature, v. 333, p. 819-824.

Brimhall, G.H., Lewis, C.J., Ford, C., Bratt, J., Taylor, G., and Warin, O., 1991a, Quantitative geochemical approach to pedogenesis: importance of parent material reduction, volumetric expansion, and eolian influx in laterization: Geoderma, v. 51, p. 51-91.

Brimhall, G.H., Chadwick, O.A., Lewis, C.J., Compston, W., Williams, I.S., Danti, K.J., Dietrich, W.E., Power, M., Hendricks, D., and Bratt, J., 1991b, Deformational mass transfer and invasive processes in soil evolution: Science, v. 255, p. 695-702.

Burgess, S.D., Bowring, S., and Shen., S., 2014, High-precision timeline for Earth's most severe extinction: National Academy of Science, Proceedings, v. 111, p. 3316-3321.

Coney, L., Reimold, W.U., Hancox, P.J., Mader, D., Koeberl, C., McDonald, I., Struck, U., Vajda, V., and Kamo, S., 2007, Geochemical and mineralogical investigation of the Permian—Triassic boundary in the continental realm of the southern Karoo Basin, South Africa: Palaeoworld, v. 16, p. 67-104.

De Kock, M.O., and Kirschvink, J.L., 2004, Paleomagnetic constraints on the Permian-Triassic Boundary in terrestrial strata of the Karoo Supergroup, South Africa: Implications for causes of the End-Permian extinction event, Gondwana Research, v. 7, p. 175-183.

DiMichele, W.A., and Gastaldo, R.A., 2008, Plant paleoecology in deep time: Missouri Botanical Garden Annals, v. 95, p. 144-198.

Driese, S.G., 2004, Pedogenic translocation of Fe in modern and ancient Vertisols and implications for interpretations of the Hekpoort paleosols (2.25 Ga): Journal of Geology, v. 112, p. 543-560.

Driese, S.G., Mora, C.I., Stiles, C.A., Joeckel, R.M., and Nordt, L.C., 2000, Mass-balance reconstruction of a modern Vertisol: implications for interpreting the geochemistry and burial alteration of paleo-Vertisols, Geoderma, v. 95, p. 179-204.

Driese, S.G., Nordt, L.C., Lynn, W.C., Stiles, C.A., Mora, C.I., and Wildings, L.P., 2005, Distinguishing climate in the soil record using chemical trends in a Vertisol climosequence from the Texas coast prairie, and application to interpreting Paleozoic paleosols in the Appalachian Basin, U.S.A.: Journal of Sedimentary Research, v. 65, p. 339-349.

Erwin, D.H., 1994, The Permo—Triassic extinction, Nature, v. 367, no. 6460, p. 231-236.

Gastaldo, R.A., and Demko, T.M., 2011, The relationship between continental landscape evolution and the plant-fossil record: long term hydrology controls that plan fossil record: *in* Allison, P.A., and Bottjer, D.J., eds., Taphonomy, Second Edition: Processes and Bias Through Time: Springer, The Netherlands, Topics in Geobiology, v. 32, p. 249-286.

Gastaldo, R.A., Adendorff, R., Bamford, M., Labandeira, C.C., Neveling, J., and Sims, H., 2005, Taphonomic trends of macrofloral assemblages across the Permian-Triassic boundary, Karoo Basin, South Africa: Palaios, v. 20, p. 479-497.

Gastaldo, R.A., Kamo, S.L., Neveling, J., Geissman, J.W., Bamford, M., and Looy, C.V., 2015, Is the vertebrate-defined Permian—Triassic boundary in the Karoo Basin, South Africa, the terrestrial expression of the end-Permian marine event?: Geology, v. 43, p. 939-942.

Gastaldo, R.A., Knight, C.L., Neveling, J., and Tabor, N.J., 2014, Latest Permian paleosols from Wapadsberg Pass, South Africa: Implications for Changhsingian climate: Geological Society of America Bulletin, v. 126, p. 665-679.

Gastaldo, R. A., Neveling, J., Clark, K., and Newbury, S.S., 2009, The terrestrial Permian—Triassic boundary event bed is a non-event: Geology, v. 37, p. 199-202.

Gastaldo, R.A., Neveling, J., Geissman, J.W., and Jiawen, L., 2018, A multidisciplinary approach to review the vertical and lateral facies relationships of the purported vertebrate-defined terrestrial Permian-Triassic boundary interval at Bethulie, Karoo Basin, South Africa, Earth-Science Reviews, doi: 10.1016/j.earscirev.2017.08.002.

Johnson, M.R., van Vuuren, C.J., Visser, J.N.J., Cole, D.I., Wickens, H. de V., Christie, A.D.M., Roberts, D.L., and Brandl, G., 2006, Sedimentary rocks of the Karoo Supergroup *in* Johnson, M.R., Anhaeusserm C.R., and Thomas, R.J., Eds., The Geology of South Africa: Geological Society of South Africa, Johanesburg, Council for Geoscience, Pretoria, p. 461-479; 492-495.

Knoll, A.H., Bambach, R.K., Canfield, D.E., and Grotzinger, J.F., 1996, Comparative Earth history and the Late Permian mass extinction: Science, v. 273, p. 452-457.

Knight, C., 2010, Late Permian paleoenvironmental factors expounded through analysis of a forest-floor paleosol profile, Karoo Basin, South Africa: Honors Theses, paper 584.

Kus, K.B., Gastaldo, R. A., Neveling, J., Geissman, J.W., and Looy, C.V., 2017, Calcisols, palynofloras, and rare charcoal from Quaggasfontein, Eastern Cape Province, South Africa: Correlations in the Wapadsberg Pass area and implications for Late Permian climate: Geological Society of America Abstracts with Programs. v. 49, doi: 10.1130/abs/2017AM-303520

Li, J., Gastaldo, R.A., Neveling, J., and Geissman, J.W., 2017, Siltstones across the *Daptocephalus (Dicynodon)* and (*Lystrosaurus*) Assemblage Zones, Karoo Basin, South Africa, show no evidence for aridification: Journal of Sedimentary Research, v. 87, p. 653-671.

Machette, M.N., 1985, Calcic soils of southwestern United States: Geological Society of America Special Paper, v. 203, p. 1-21.

Mack, G.H., James, W.C., and Monger, H.C., 1993, Classification of paleosols: Geological Society of America Bulletin, v. 105, p. 129-136.

MacLeod, K.G., Smith, R.M.H., Koch, P.L., and Ward, P.D., 2000, Timing of mammal-like-reptile extinctions across the Permian-Triassic boundary in South Africa: Geology, v. 28, p. 227-230.

MacLeod, K.G., Quinton, P.C., and Bassett, D.J., 2017, Warming and increased aridity during the earliest Triassic in the Karoo Basin, South Africa, Geology, v. 45, no. 6, p. 483-486.

Maruoka, T., Koeberl, C., Hancox, P.J., and Reimold, W.U., 2002, Sulfur geochemistry across a terrestrial Permian-Triassic boundary section in the Karoo Basin, South Africa: Earth and Planetary Science Letters, v. 206, p. 101-117.

Nordt, L., Orosz, M., Driese, S., and Tubbs, J., 2006, Vertisol carbonate properties in relation to mean annual precipitation: implications for paleoprecipitation estimates: Journal of Geology, v. 114, p. 501-510.

Payne, J.L., and Clapham, M.E., 2012, End-Permian Mass Extinction in the oceans: an acient analog for the twenty-first century?: Annual Review of Earth and Planetary Sciences, v. 40, p. 89-111.

Pace, D.W., Gastaldo, R.A., and Neveling, J., 2009, Aggradational and deagradational landscapes in the Early Triassic of the Karoo Basin and evidence for dramatic climate shifts following the P/Tr event: Journal of Sedimentary Research, v. 79, p. 276-291.

Prevec, R., Gastaldo, R.A., Looy, C.V., Neveling, J., and Reid, B.S., 2010, An autochthonous glossoperid flora with Latest Permian palynomorphs and its depositional setting from the *Dicynodon* assemblage zone of the southern Karoo Basin, South Africa: Palaeogeography, Palaeoclimatology, Palaeoecology, v. 292, p. 381-408.

Retallack, G.J., Smith, R.M.H., and Ward, P.D., 2003, Vertebrate extinction across Permian-Triassic boundary in Karoo Basin, South Africa: Geological Society of America Bulletin, v. 115, p. 1133-1152.

Reichow, M.K., Pringle, M.S., Al'Mukhamedov, A.I., Allen, M.B., Andreichev, V.L., Buslov, M.M., Davies, C.E., Fedoseev, G.S., Fitton, J.G., Inger, S., Medvedev, A.Ya., Mitchell, C., Puchkov, V.N., Safonova, I.Yu., Scott, R.A., and Saunders, A.D., 2009, The timing and extent of the eruption of the Siberian Traps large igneous province: Implications for the end-Permian environmental crisis: Earth and Planetary Science Letters, v. 277, p. 9-20.

Sheldon, N.D., 2005, Do red beds indicate paleoclimatic conditions?: a Permian case study: Palaeogeography, Palaeoclimatology, Palaeoecology, v. 228, p. 305-319.

Sheldon, N.D., and Tabor, N.J., 2009, Quantitative paleoenvironmental and paleoclimatic reconstruction using paleosols: Earth Science Reviews, v. 95, p. 1-52.

Sheldon, N.D., Retallack, G.J., and Tanaka, S., 2002, Geochemical climofunctions from North American soils and application to paleosols across the Eocene-Oligocene boundary in Oregon: Journal of Geology, v. 110, p. 687-696.

Smith, R.M., 1990, Alluvial paleosols and pedofacies sequences in the Permian Lower Beaufort of the southwestern Karoo Basin, South Africa: Journal of Sedimentary Research, v. 60, p. 258-276.

Smith, R.M.H., 1995, Changing fluvial environments across the Permian-Triassic boundary in the Karoo Basin, South Africa, and possible causes of the extinctions: Palaeogeography, Palaeoclimatology, Palaeoecology, v. 117, p. 81-104.

Smith, R.M.H., and Botha, J., 2005, The recovery of terrestrial vertebrate diversity in the South African Karoo Basin after the end-Permian Extinction: Compte Rendu Palevol, v. 4, p. 555-568.

Smith, R.M.H., and Botha-Brink, J., 2014, Anatomy of a mass extinction: Sedimentological and taphonomic evidence for drought-induced-die-offs at the Permo-Triassic boundary in the main Karoo Basin, South Africa: Palaeogeography, Palaeoclimatology, Palaeoecology, v. 396, p. 99-118.

Smith, R.M.H., Eriksson, P.G., and Botha, W.J., 1993, A review of the stratigraphy and sedimentary environments of the Karoo-aged basins of Southern Africa: Journal of African Earth Sciences, v. 16, no. ½, p. 143-169.

Smith, R.M.H., and Ward, P.D., 2001, Pattern of vertebrate extinctions across an event at the Permian-Triassic boundary in the Karoo Basin of South Africa: Geology, v. 29, p. 1147-1150, doi:10.1130/0091-7613(2001)029<1147:POVEAA>2.0CO;2.

Stiles, C.A., Mora, C.I., and Driese, S.G., 2003, Pedogenic processes and domain boundaries in a Vertisol climosequence: eveidencefromtitanium and zirconium distribution and morphology: Geoderma, v. 116, p. 279-299.

Stiles, C.A., Mora, C.I., Driese, S.G., and Robinson, A.C., 2003, Distinguishing climate and time in the soil record: Mass-balance trends in Vertisols from the Texas coastal prairie: Geological Society of America, v. 31, p. 331-334.

Thomas, S.G., Tabor, N.J., Yang, W., Myers, T.S., Yang, Y., and Wang, D., 2011, Palaeosol stratigraphy across the Permian-Triassic boundary, Bogda Mountains, NW China: implications for palaeoenvironmental transition through earth's largest mass extinction: Palaeogeography, Palaeoclimatology, Palaeoecology, v. 308, p. 41-64.

Viglietti, P.A., Smith, R.M.H., Angielczyk, K.D., Kammerer, C.F., Fröbisch, J., and Rubidge, B.S., 2016, The *Daptocephalus* Assemblage Zone (Lopingian), South Africa: A proposed biostratigraphy based on a new compilation of stratigraphic ranges: Journal of African Earth Sciences, v. 113, p. 153-164.

Viglietti, P.A., Smith, R.M.H., and Rubidge, B.S., 2018, Changing palaeoenvironments and tetrapod populations in the *Daptocephalus* Assemblage Zone (Karoo Basin, South Africa) indicate early onset of the Permo-Triassic mass extinction: Journal of African Earth Sciences, v. 138, p. 102-111.

Ward, P.D., Montgomery, D.R., and Smith, R.M.H., 2000, Altered river morphology in South Africa related to the Permian-Triassic extinction: Science, v. 289, p. 1740-1743, doi:10.1126/science.289.5485.1740.

Ward, P.D., Botha, J., Buick, R., DeKock, M.O., Erwin, D.H., Garrison, G., Kirschvink, J., and Smith, R.M.H., 2005, Abrupt and gradual extinction among Late Permian land vertebrates in the Karoo Basin, South Africa: Science, v. 307, p. 709-714, doi:10.1126/science.1107068.

Wignall, P.B., Twitchett, R.J., 1996, Oceanic anoxia and the end-Permian mass extinction: Science, v. 272, p. 1155-1158.

FIGURES

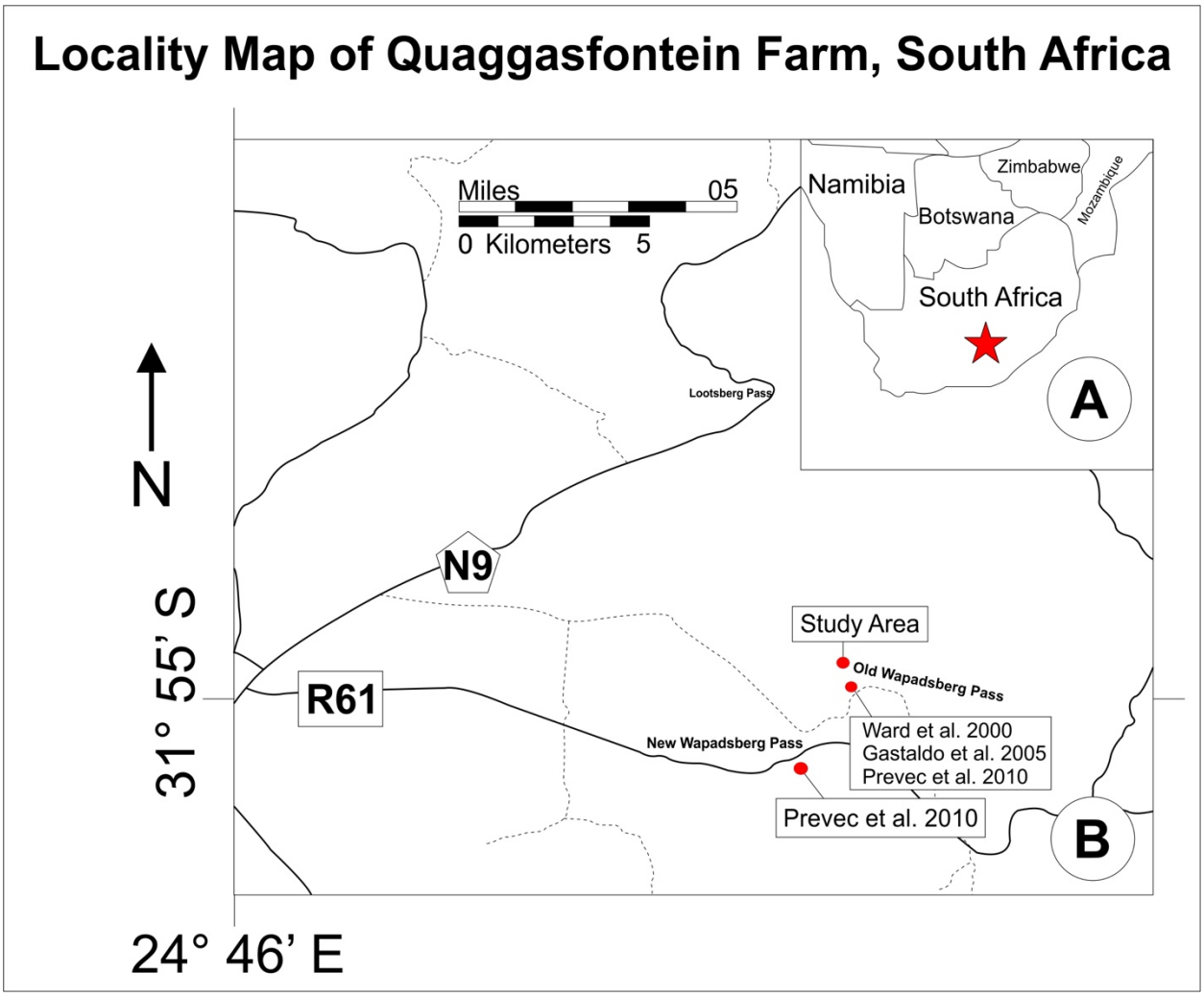

Figure 1. Geographic location of Wapadsberg Pass, Eastern Cape Province, South Africa. (A) Map of South Africa on which the general location of the study area is marked with a star. (B) Road map of the Eastern Cape Province showing the general Wapadsberg Pass area.

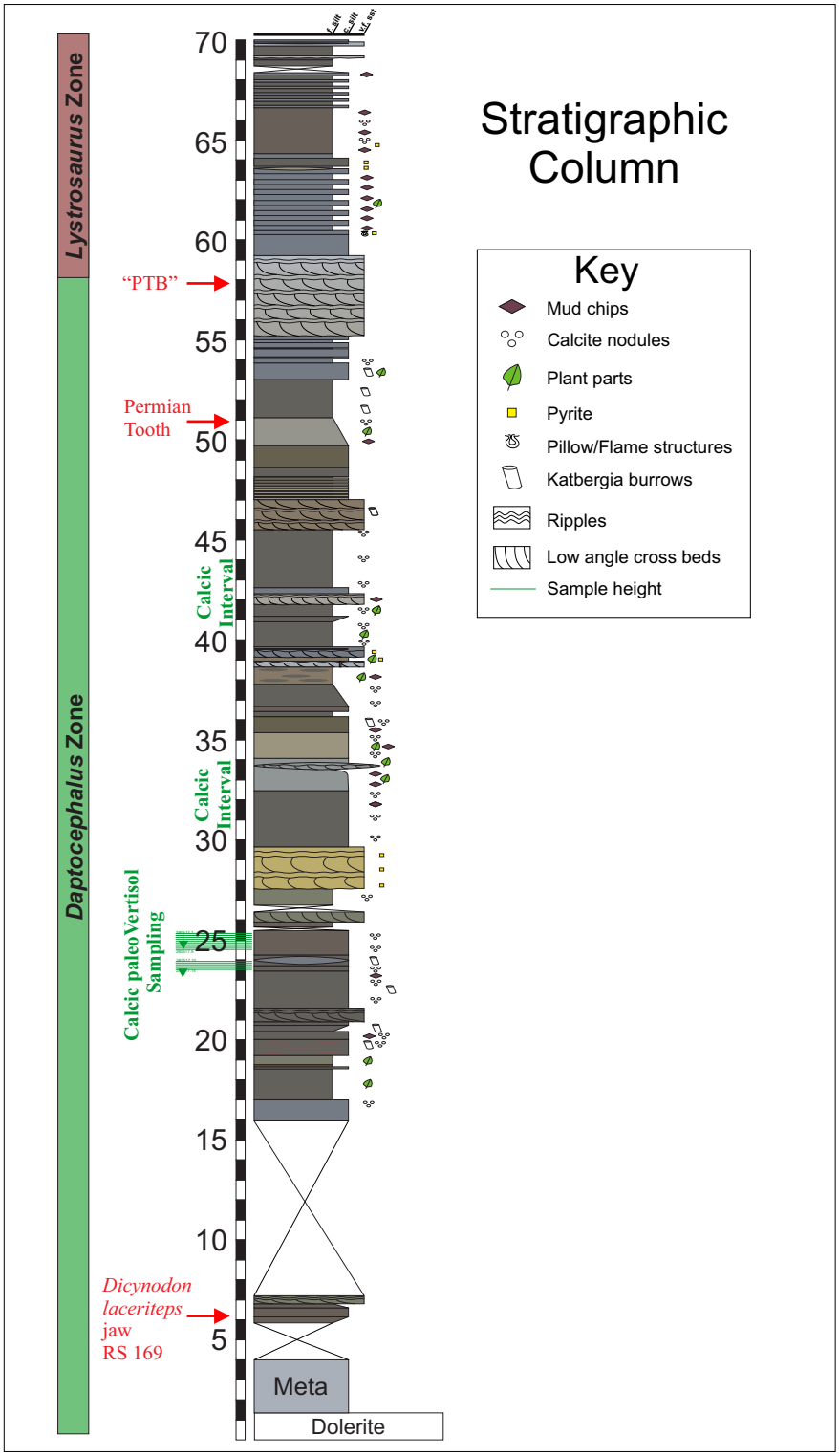

Figure 2. Stratigraphic column of Kus et al. (2017) showing the position of the Permian-age skull reported by Smith and Botha-Brink (2014), the gorgonopsian tooth, and the vertebrate-defined PTB (Smith and Botha-Brink, 2014) in relation to the sampled calcic Vertisol interval. Other intervals of less well-developed calcic nodular horizons are also labeled. The colors are representative of the Munsell color of the rocks reported in the field. Scale in meters.

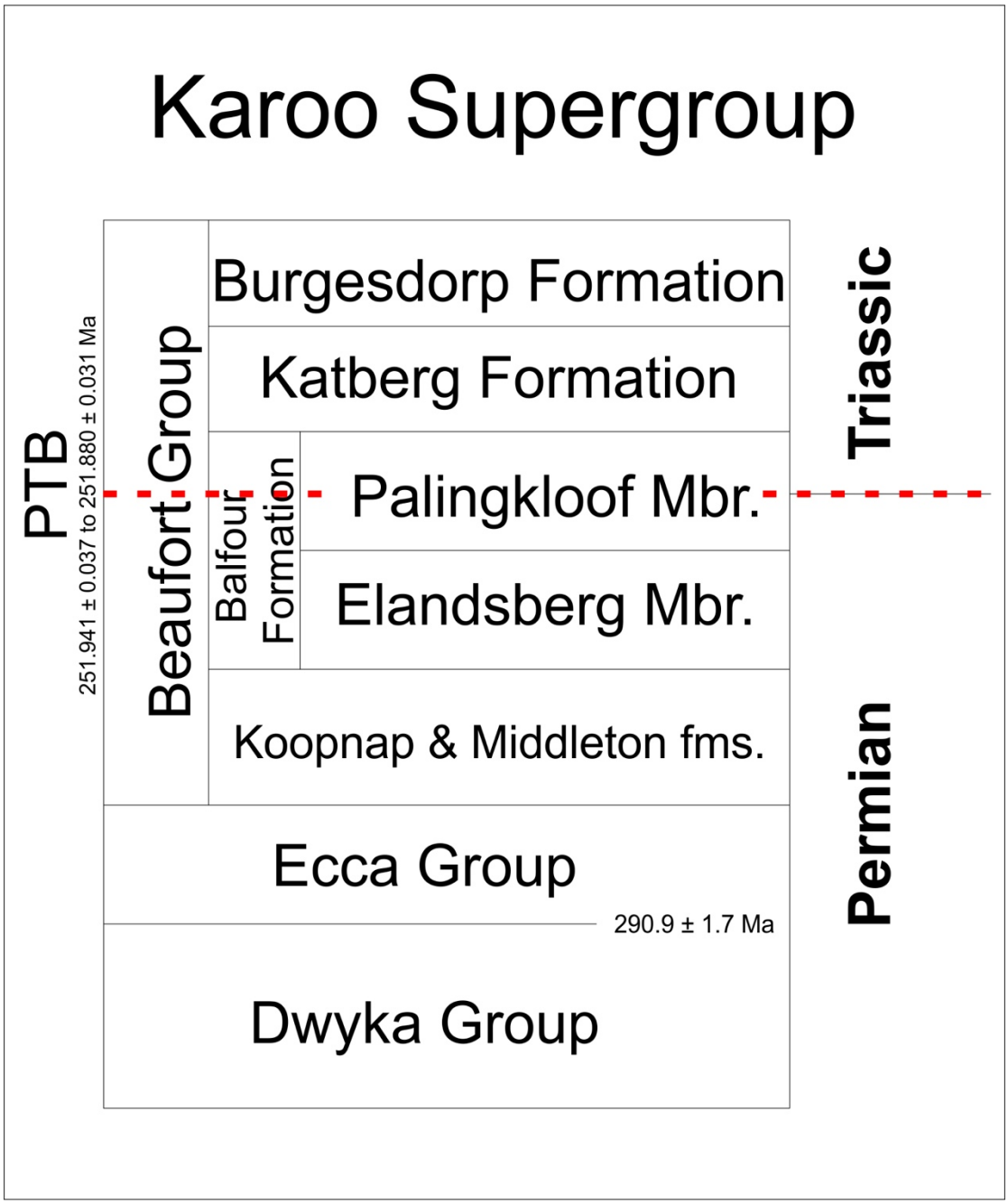

Figure 3. Generalized stratigraphy of the Karoo Basin, South Africa. The chronometric age for the PTB in the marine realm is from Burgess et al. (2014). PTB placement after model proposed by Smith and Botha-Brink (2014).

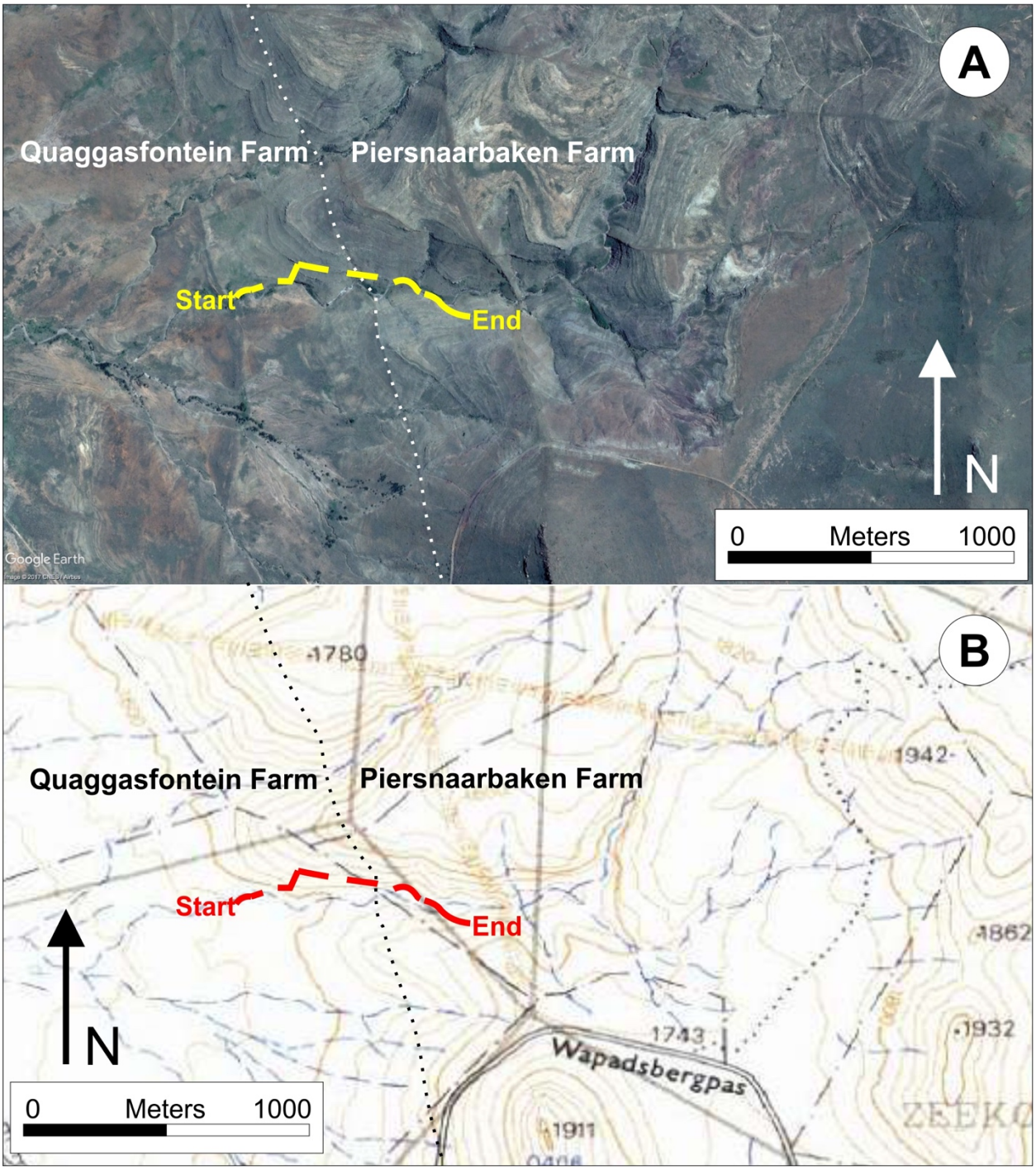

Figure 4. Path traversed to measure 70-m stratigraphic section. (A) Image from Google Earth with solid yellow lines representing measured section. Dashed yellow lines represent the path walked to reach a correlative bed (no stratigraphy measured). This was necessary because of loss of rock exposure in some portions of the donga. Dotted line (white) delineates the fence-line between Quaggasfontein and Piersnaarbaken farms. (B) Topographic map from Spatial Reference (www.spatialreference.co.za) showing the same location and path traveled (red). Dotted line (black) delineates the fence-line between Quaggasfontein and Piersnaarbaken farms.

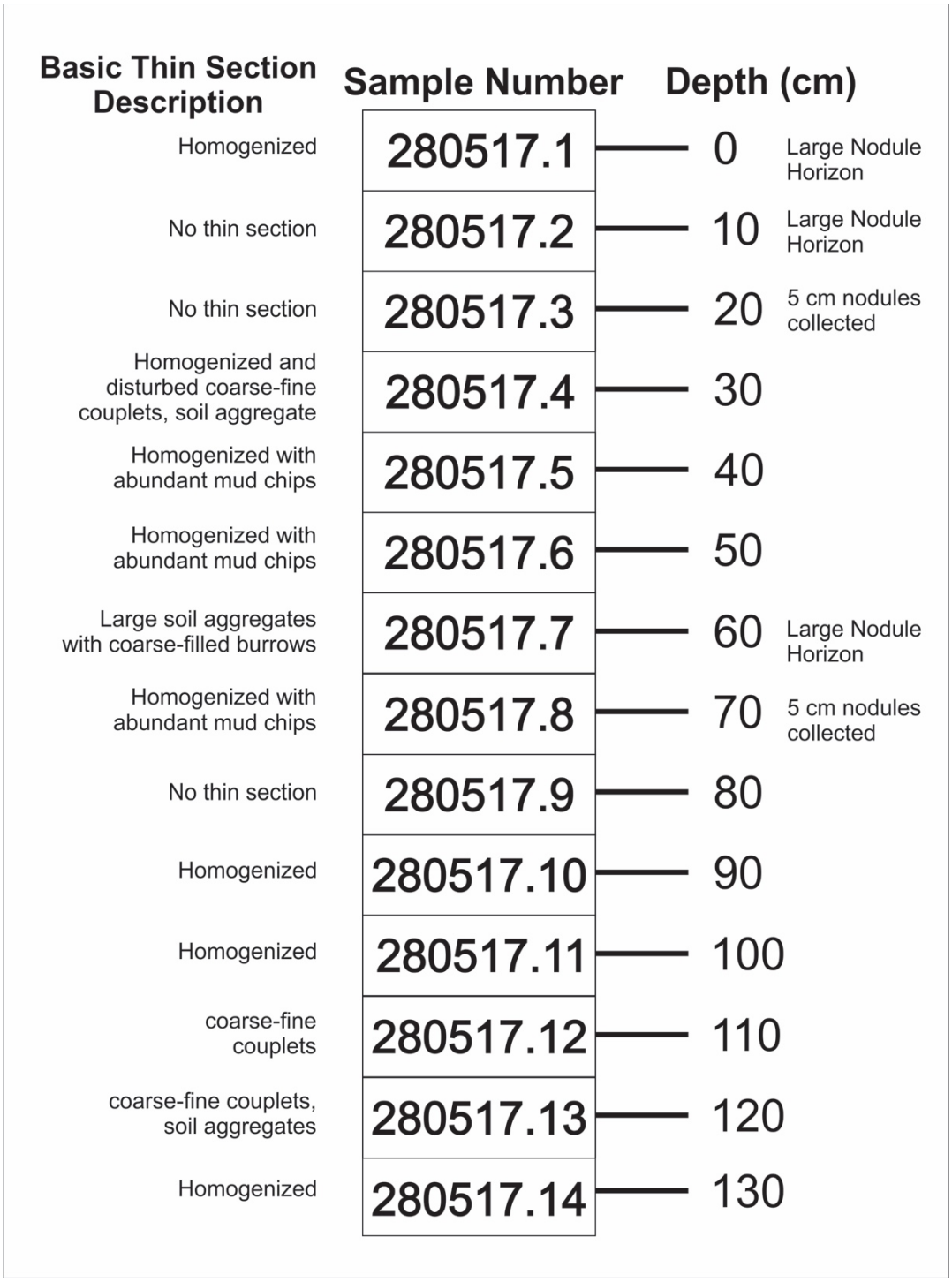

Figure 5. Generalized stratigraphy of the 1.3-m thick interval sampled for thin sections and geochemical analyses. Sample 280517.1 was collected at the top of the calcic Vertisols interval and is assigned a depth of 0 cm. Sample 280517.14 was collected at the base at a depth of 1.3 cm. All samples were collected at 10-cm intervals. A basic thin section description based on the the prominent fabric or feature(s) of the thin sections is to the left of the sample number. One-cm-diameter nodules were present throughout the interval; however, horizons of larger nodules are noted to the right beside their depths of occurrence.

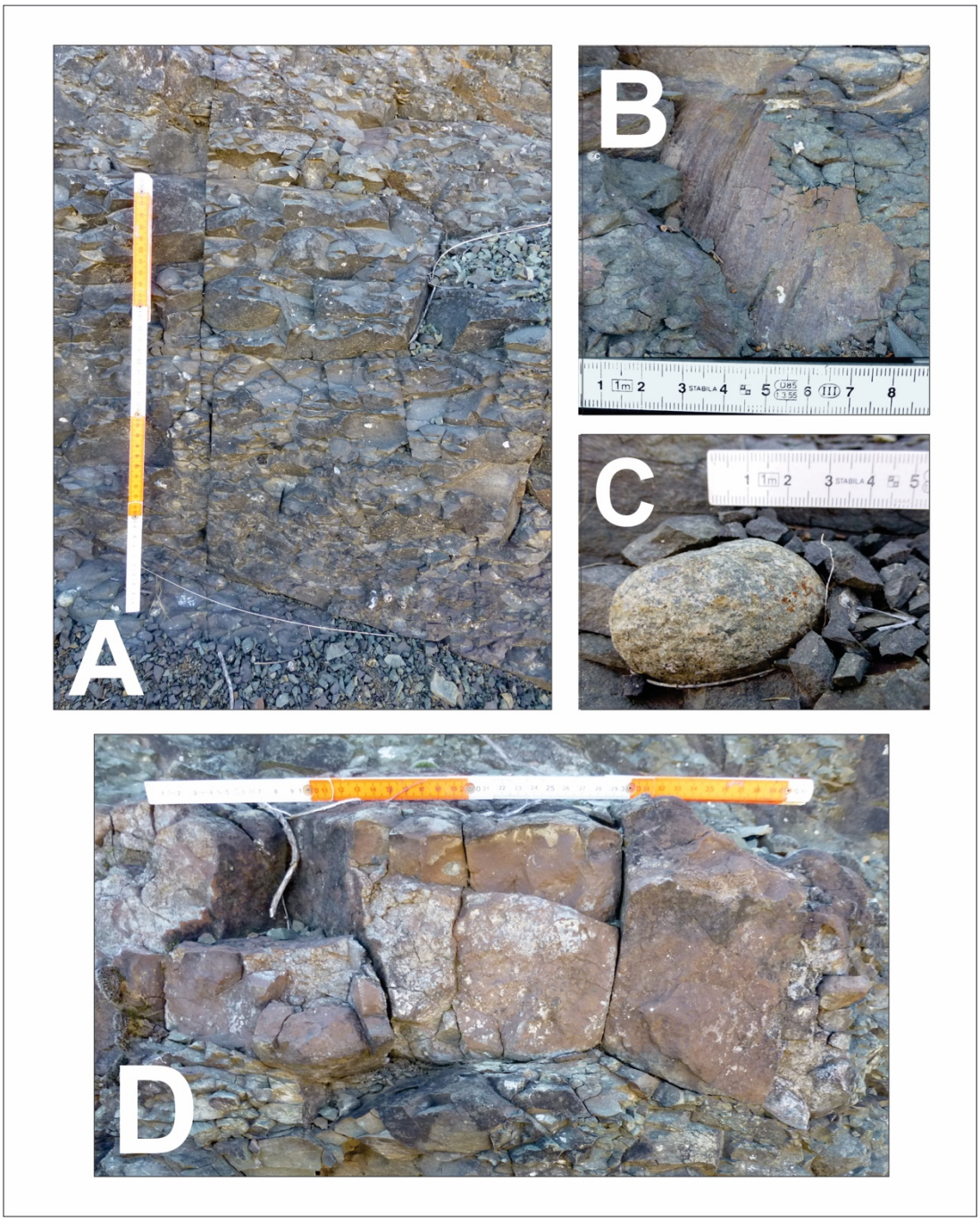

Figure 6. A. Photograph of the Lower Calcic Paleosol as identified in the field. The interval is ~80 cm thick; the lowermost 30 cm is illustrated. B. Photograph of slickensides found in a siltstone interval along the outcrop. C. Photograph of an ~5 cm elliptical carbonate-cemented nodule. D. Photograph of large nodule concretionary horizon. Nodules were found up to 20 cm in length. Scale in cm and m.

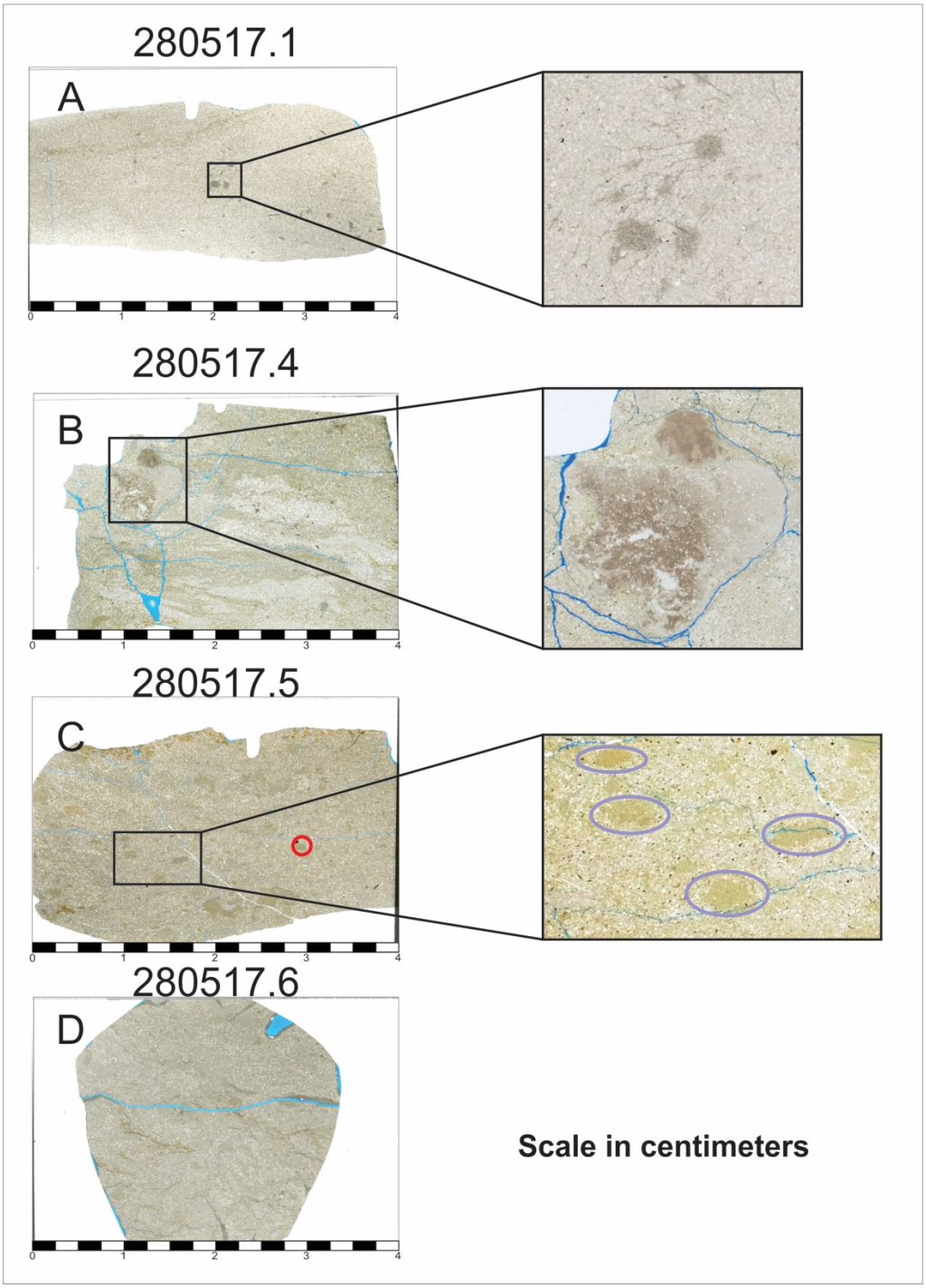

Figure 7. Photographs of calcic paleoVertisol thin sections. A. Sample 280517.1 at a depth of 0 cm shows no primary structures but contains mm-scale remnants of organic matter in the center of the slide (enlargement). B. Sample 280517.4 at a depth of 30 cm shows coarse-fine laminations that have been deformed. A large soil aggregate is visible in the upper left corner (enlargement). C. Sample 280517.5 at a depth of 40 cm shows no evidence of lamination but contains abundant mm-scale mud chips (purple circles). Sub-mm scale cubic pyrite is also visible (red circle). D. Sample 280517.6 at a depth of 50 cm is similar to sample 280517.5; however, the mud chips are less well-defined. Scales in cm.

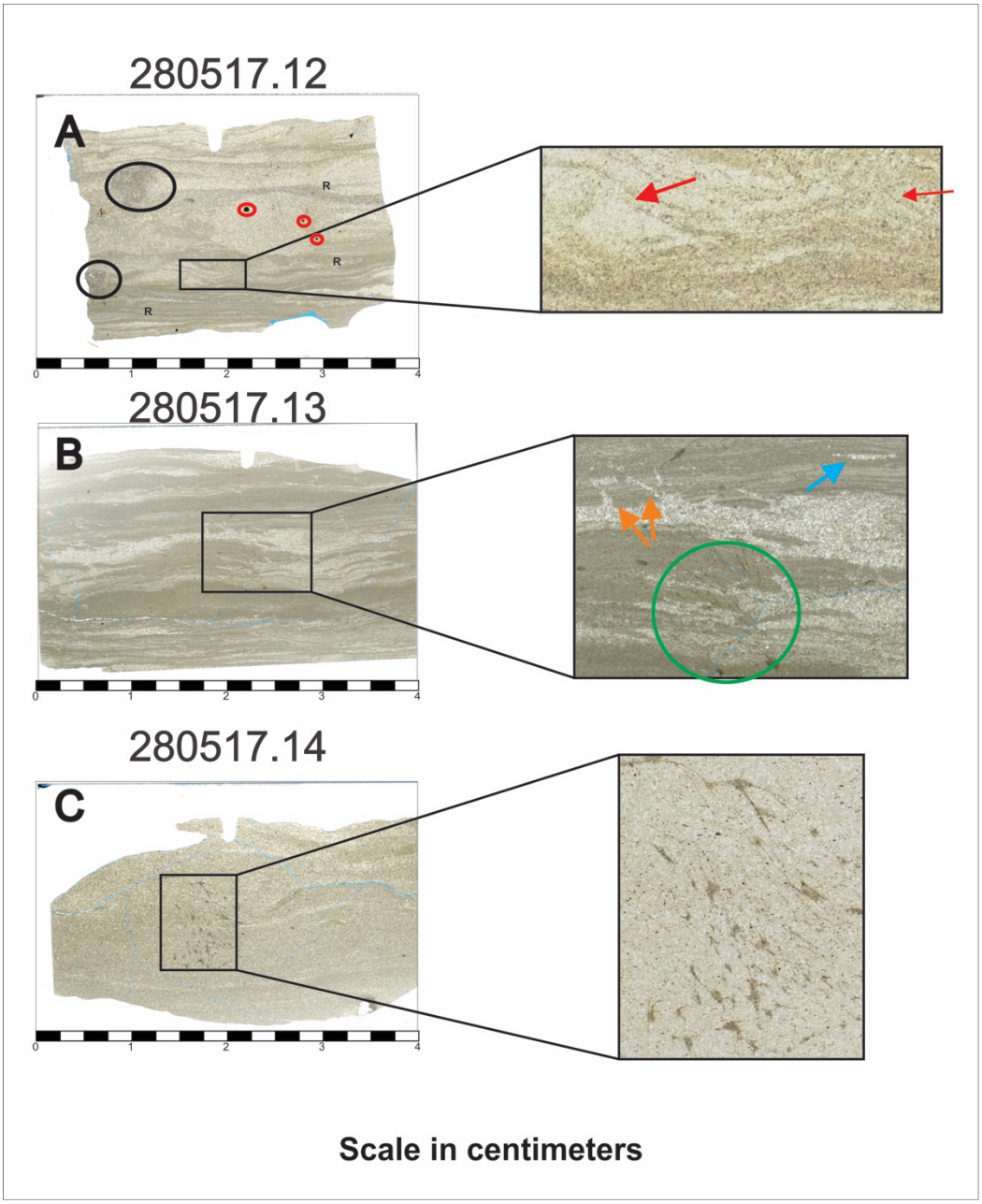

Figure 8. Photographs of calcic paleoVertisol thin sections. A. Sample 280517.12 at a depth of 110 cm has very distinct coarse-fine couplets that become thicker near the top. The coarse silt layers dominate the upper half of the thin section, and there are occasional small-scale ripples between laminations (R). Sub-mm cubic pyrite is highlighted in the red circles. Two soil aggregates (black circles) and mm-scale soft-sediment deformation (flame structures; red arrows) are also present. B. Sample 280517.13 at a depth of 120 cm displays distinct coarse-fine couplets; the finer layers tend to be thicker than the coarse layers. Sub-vertical (orange arrows) and horizontal (blue arrows) burrows—filled with coarse silt—are present. A zone of macerated plant material that radiates out of several small dark circles of concentrated organic matter (green circle) occurs at the center of the slide. C. Sample 280517.14 at a depth of 130 cm has very weakly-defined lamination. A large area of macerated plant material is visible near the center of the slide (enlargement). Scales in cm.

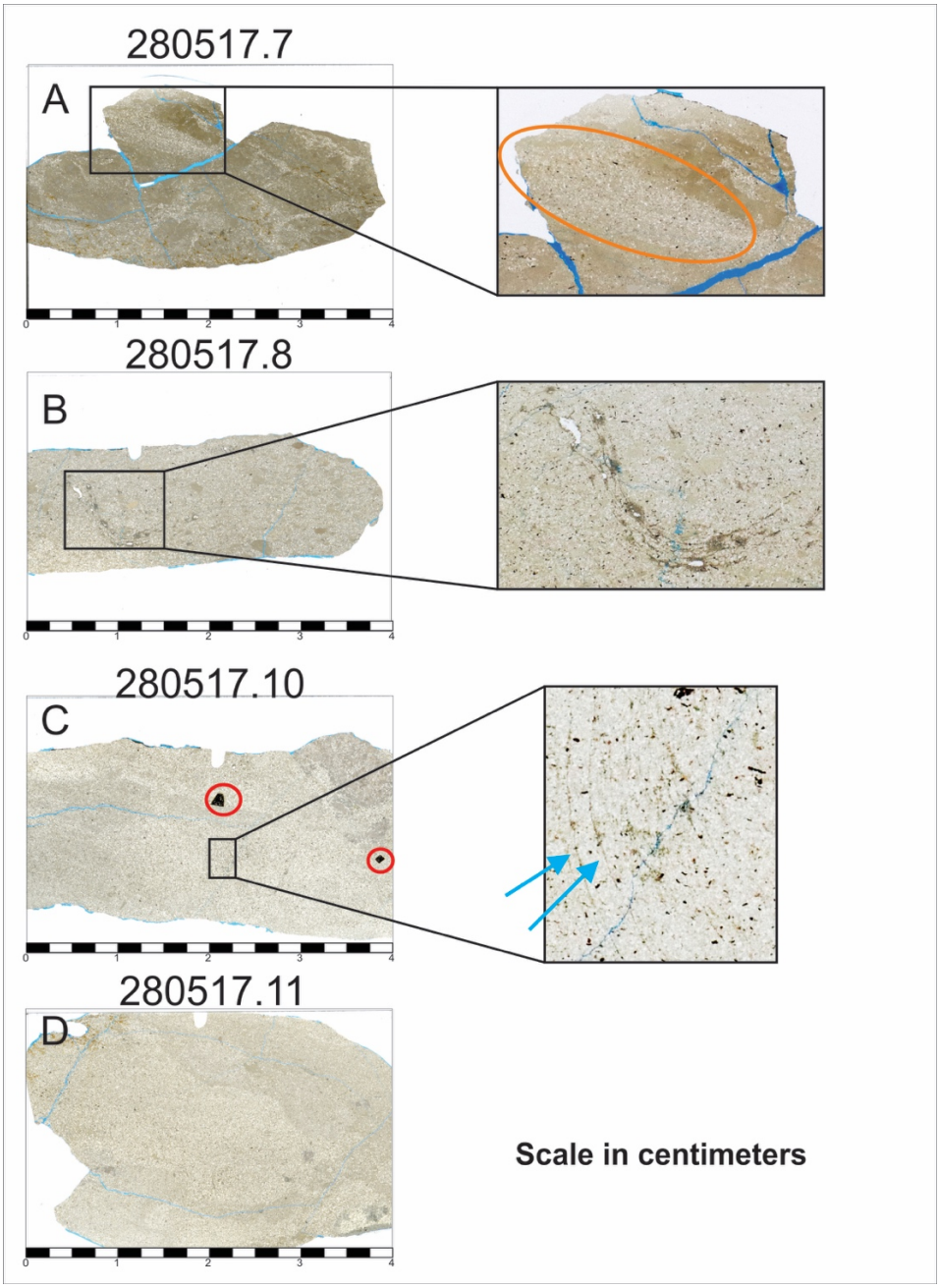

Figure 9. Photographs of calcic paleoVertisol thin sections. A. Sample 280517.7 at a depth of 60 cm contains the largest and most abundant mud clasts. A possible silt-filled burrow is outlined in orange. B. Sample 280517.8 at a depth of 70 lacks lamination but contains abundant mm-scale mud chips. The sample also contains macerated plant material in the shape of an "S" (enlargement). C. Sample 280517.10 at a depth of 90 cm contains two large cubic pyrite crystals (red circles). There is no evidence of lamination, and there are very few mud chips. There is a single soil aggregate near the top right of the slide. Near the center of the slide is evidence of macerated plant material in the form of several parallel vertical lines (blue arrows). D. Sample 280517.11 at a depth of 110 cm displays a homogenous fabric and few mud chips. Scales in cm.

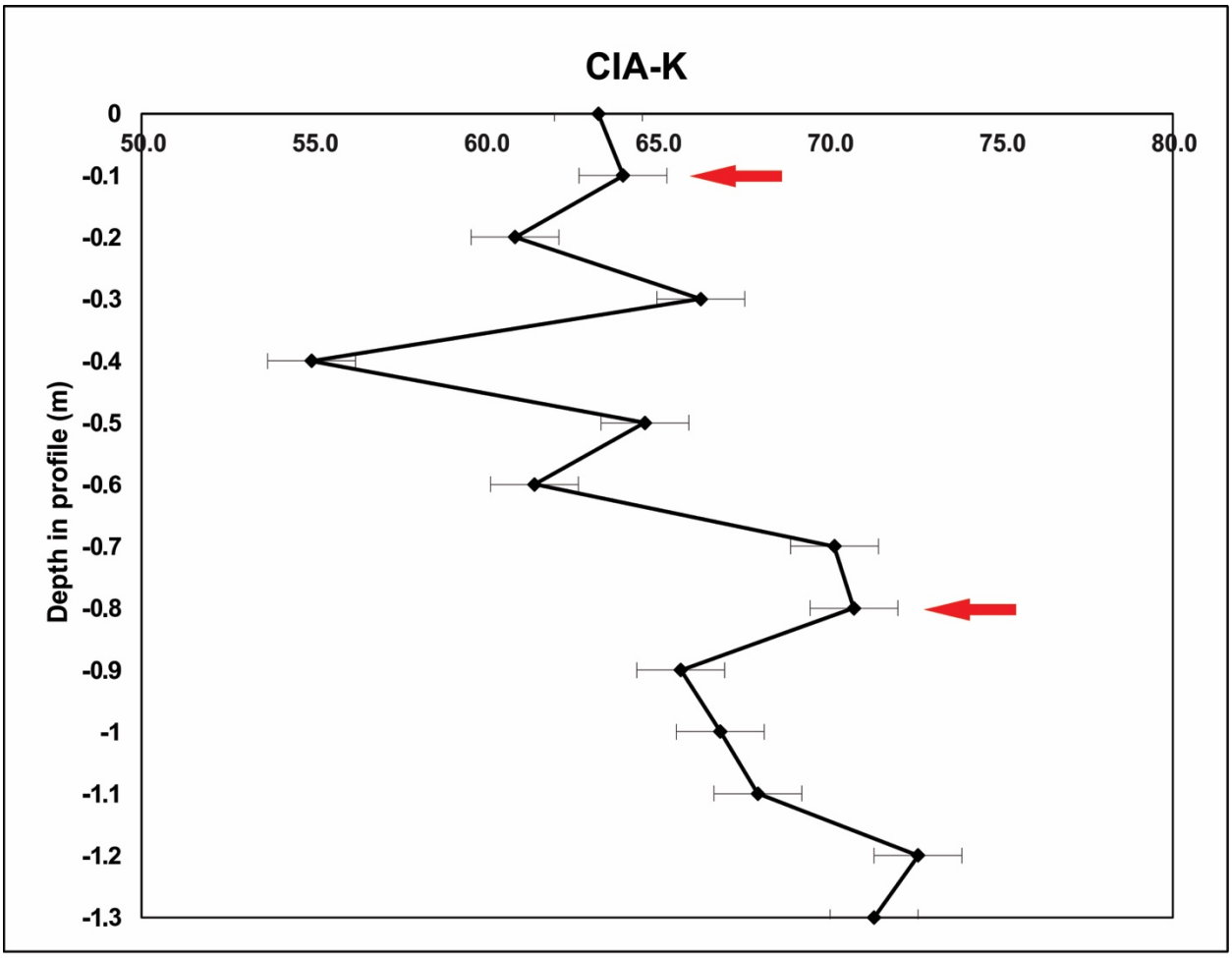

Figure 10. The Chemical Index of Alteration minus potassium vs. depth in the sampled profile. CIA-K values show an overall decreasing trend. Red arrows indicate samples and values used to calculate MAP after Sheldon and Tabor (2009).

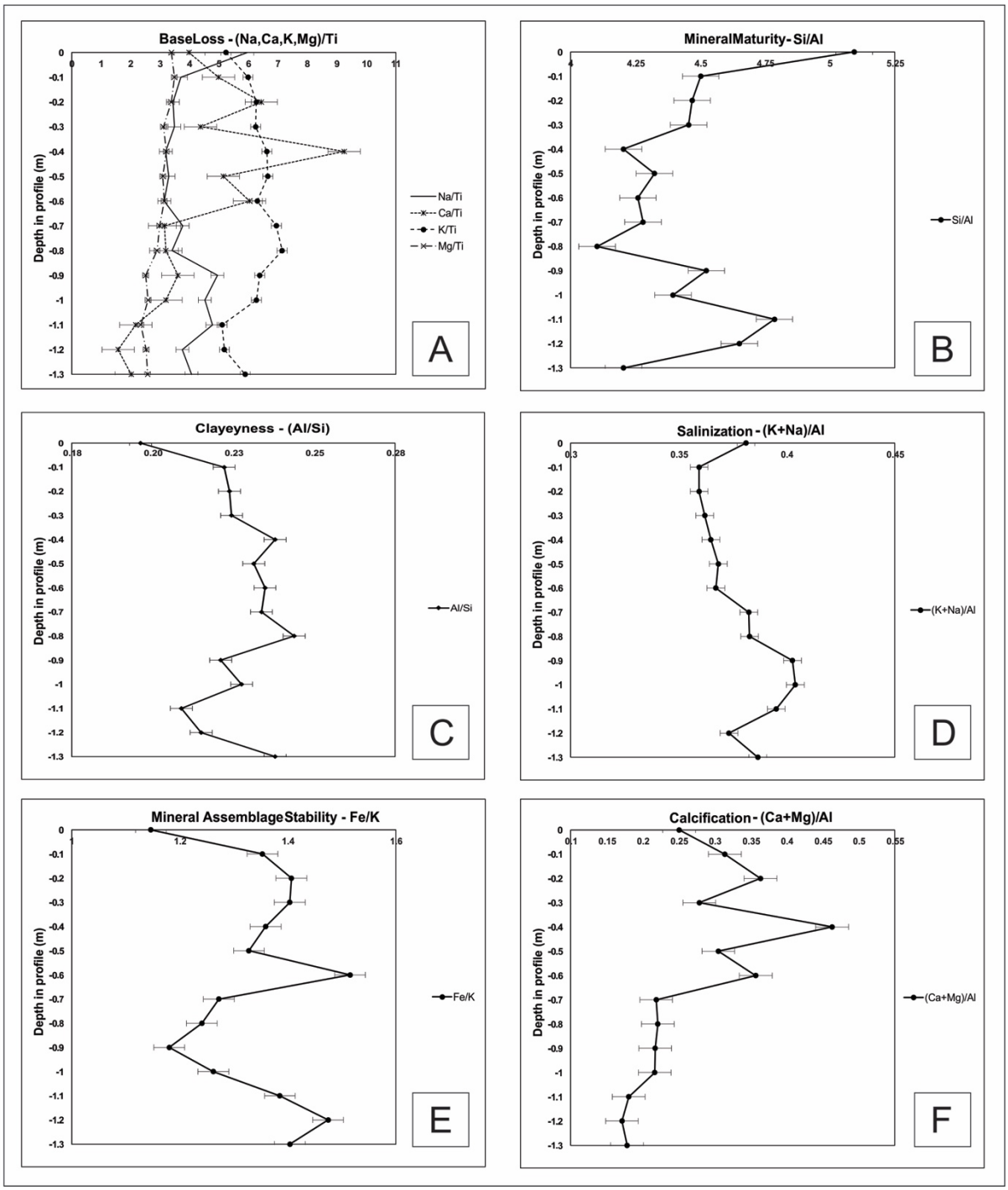

Figure 11. Six geochemical weathering proxies of the calcic paleoVertisol interval plotted against depth in profile. Standard error bars are shown for each plot. See text results and discussion. A. Base loss profiles for Mg/Ti (dashed and dotted line), Ca/Ti (short dashed line), Na/Ti (solid line), and K/Ti (long dashed line). B. Mineral maturity (Si/Al). C. Clayeyness (Al/Si). D. Salinization ([K+Na]/Al). Mineral assemblage stability (Fe/K). F. Calcification ([Ca+Mg]/Al).

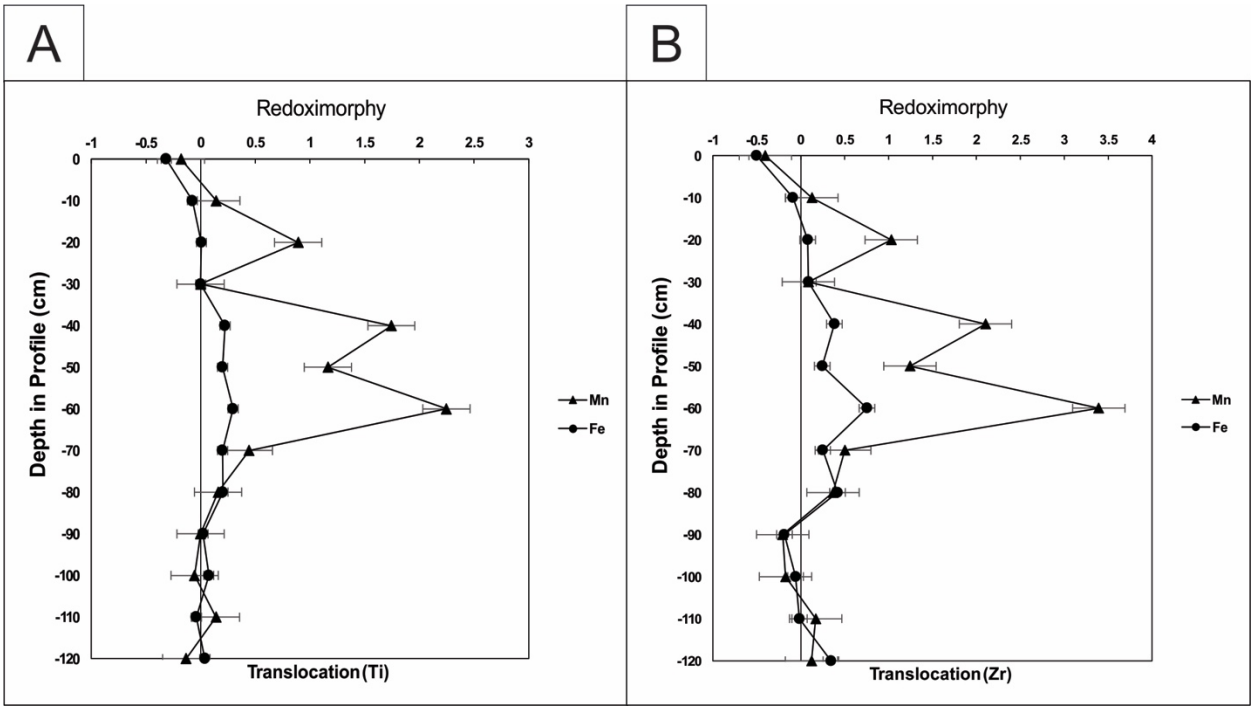

Figure 12. Translocation of Mn and Fe in the 1.3-m calcic paleoVertisol profile. Data were calculated using interpreted C-horizons at depths of 30 cm and 110-120 cm (data averaged). A. Trends plotted against depth in profile using Ti as immobile element. B. Trends plotted against depth in profile using Zr as immobile element.

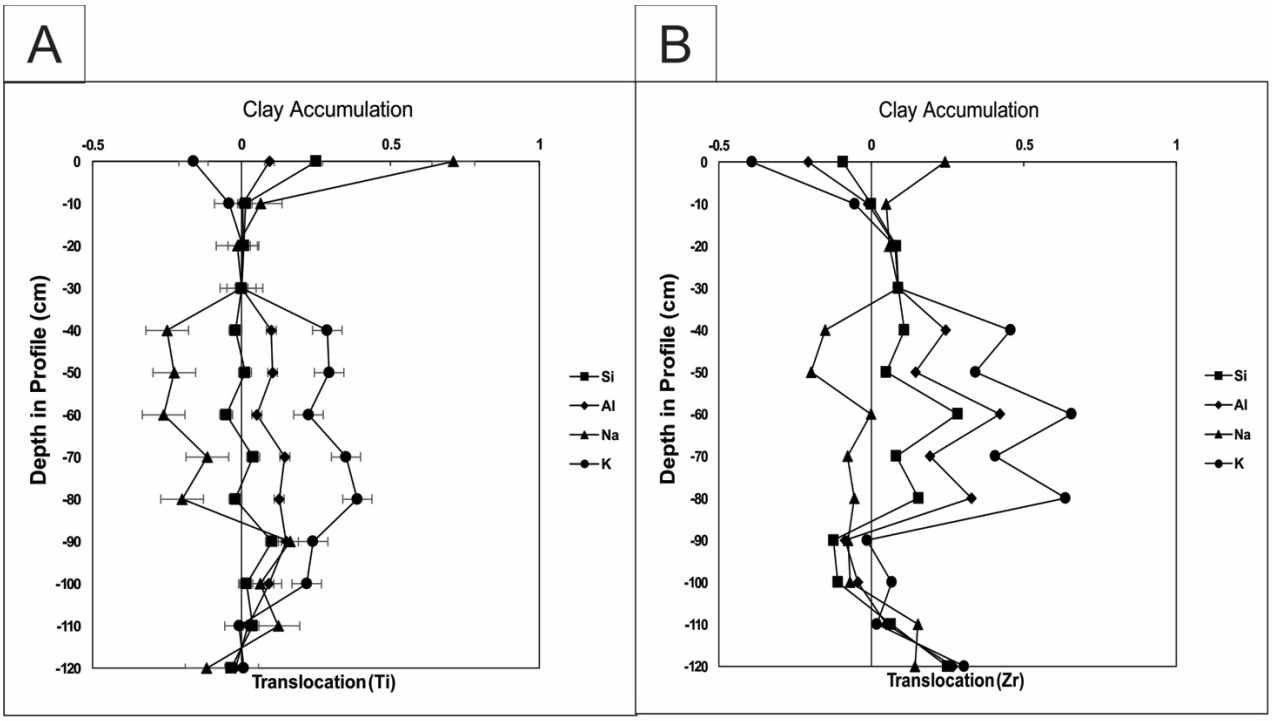

Figure 13. Translocation of Si, Al, Na and K in the 1.3-m calcic paleoVertisols profile. Data were calculated using interpreted C-horizons at depths of 30 cm and 110-120 cm (data averaged). A. Trends plotted against depth in profile using Ti as immobile element. B. Trends plotted against depth in profile using Zr as immobile element.

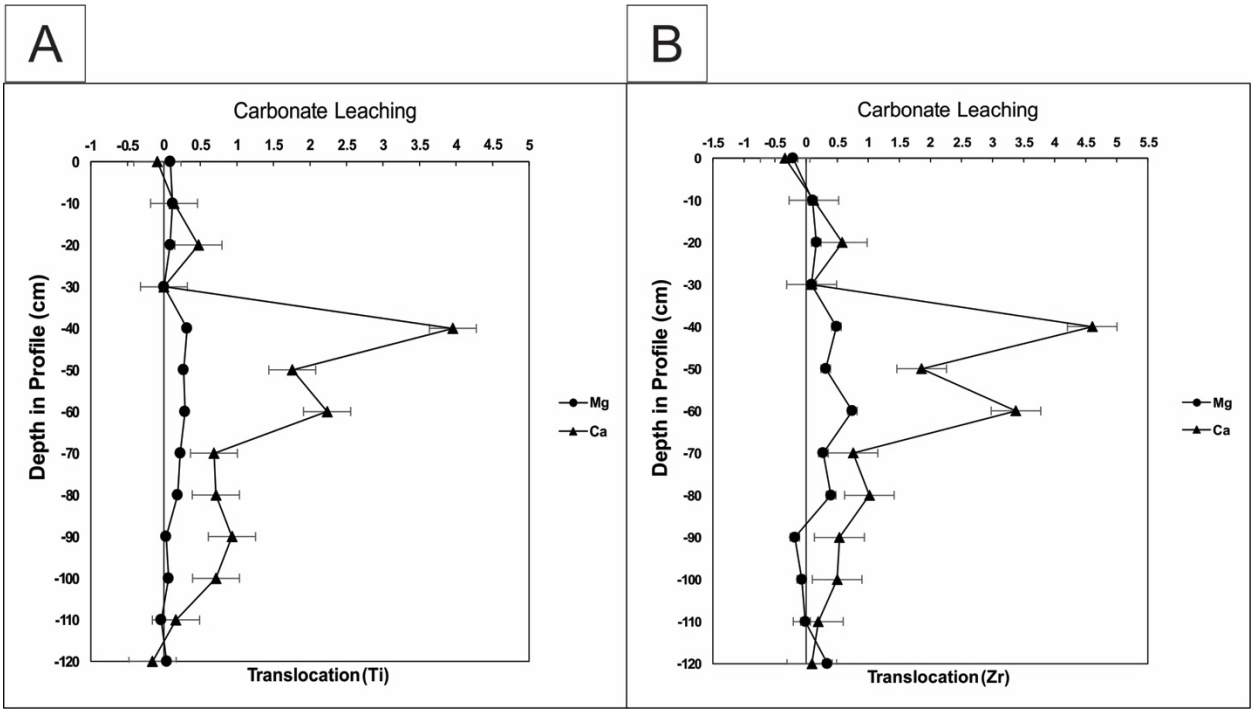

Figure 14. Translocation of Mg and Ca in the 1.3-m calcic paleoVertisol profile. Data were calculated using interpreted C-horizons at depths of 30 cm and 110-120 cm (data averaged). A. Trends plotted against depth in profile using Ti as immobile element. B. Trends plotted against depth in profile using Zr as immobile element.

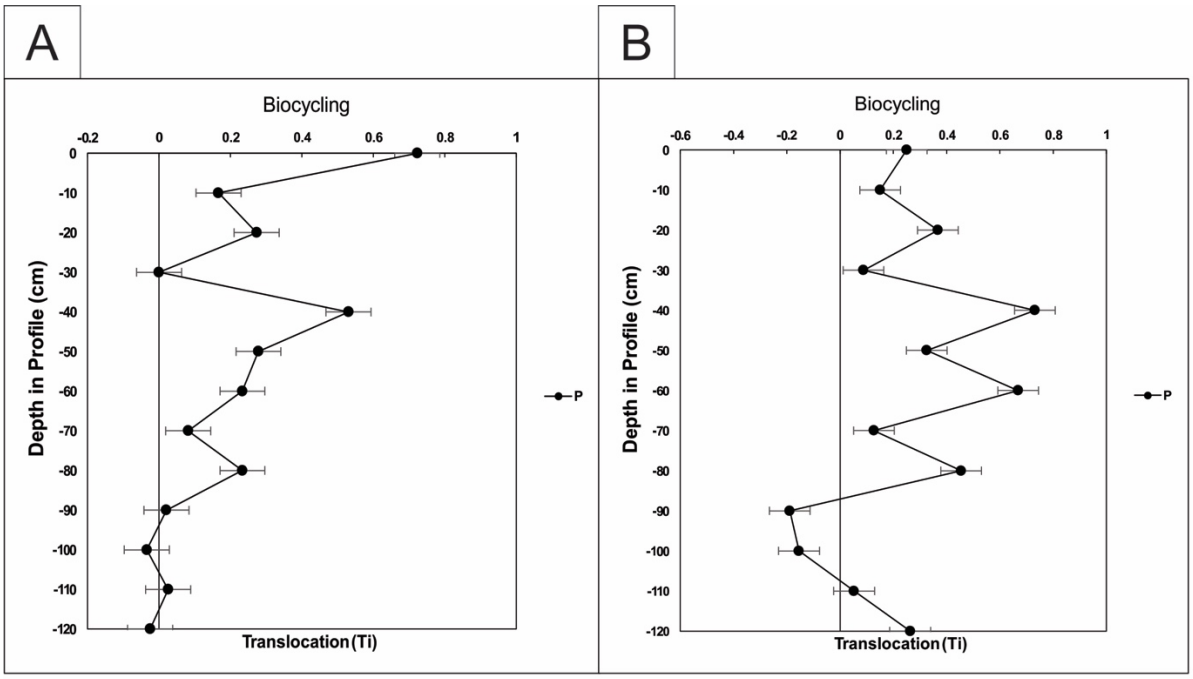

Figure 15. Translocation of P in the 1.3-m calcic paleoVertisol profile. Data were calculated using interpreted C-horizons at depths of 30 cm and 110-120 cm (data averaged). A. Trends plotted against depth in profile using Ti as immobile element. B. Trends plotted against depth in profile using Zr as immobile element.

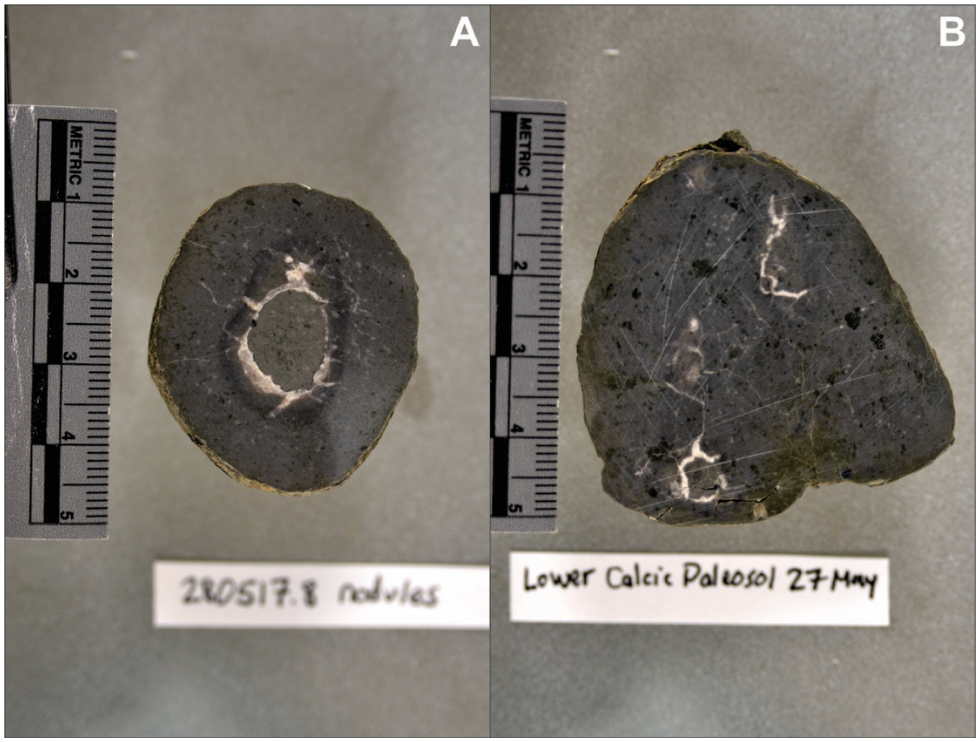

Figure 16. Photographs of nodules with septarian cracks taken from the Lower Calcic Paleosol (LCP) at a depth of 70 cm in the profile (see Fig. 5). Nodules have a micritic fabric around calcite spar. A. There is a dark grey corona around the septarian crack.

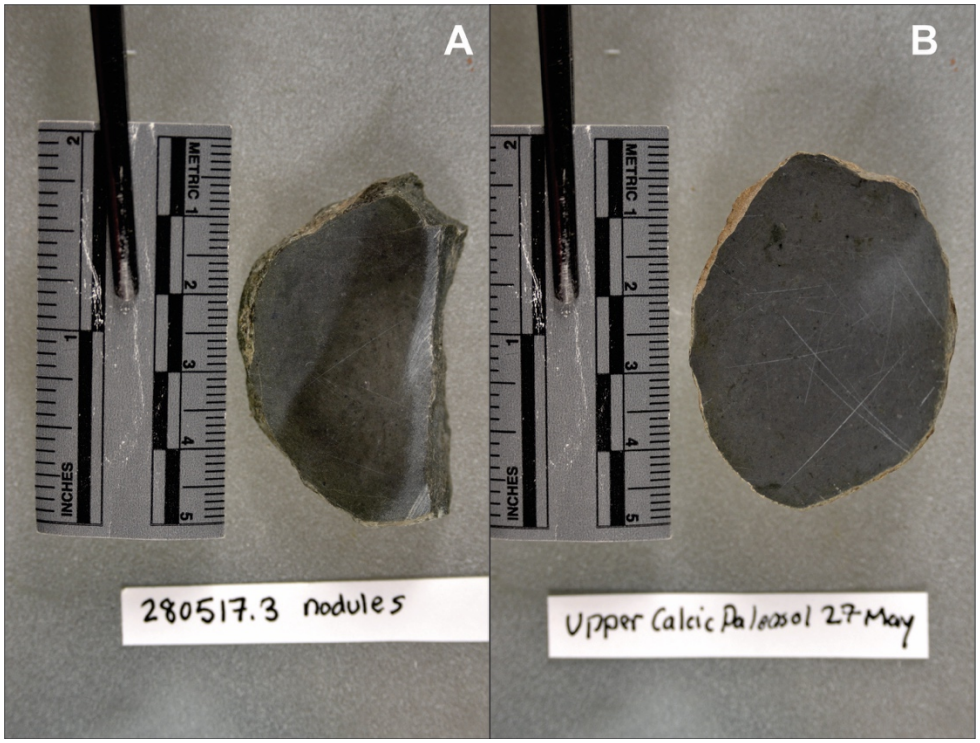

Figure 17. Photographs of two nodules from the Upper Calcic Paleosol (UCP) taken at a depth of 20 cm in the profile (Fig. 5). These nodules are elliptical in shape and have a micritic fabric. No large calcite spar is visible in slabbed hand sample.

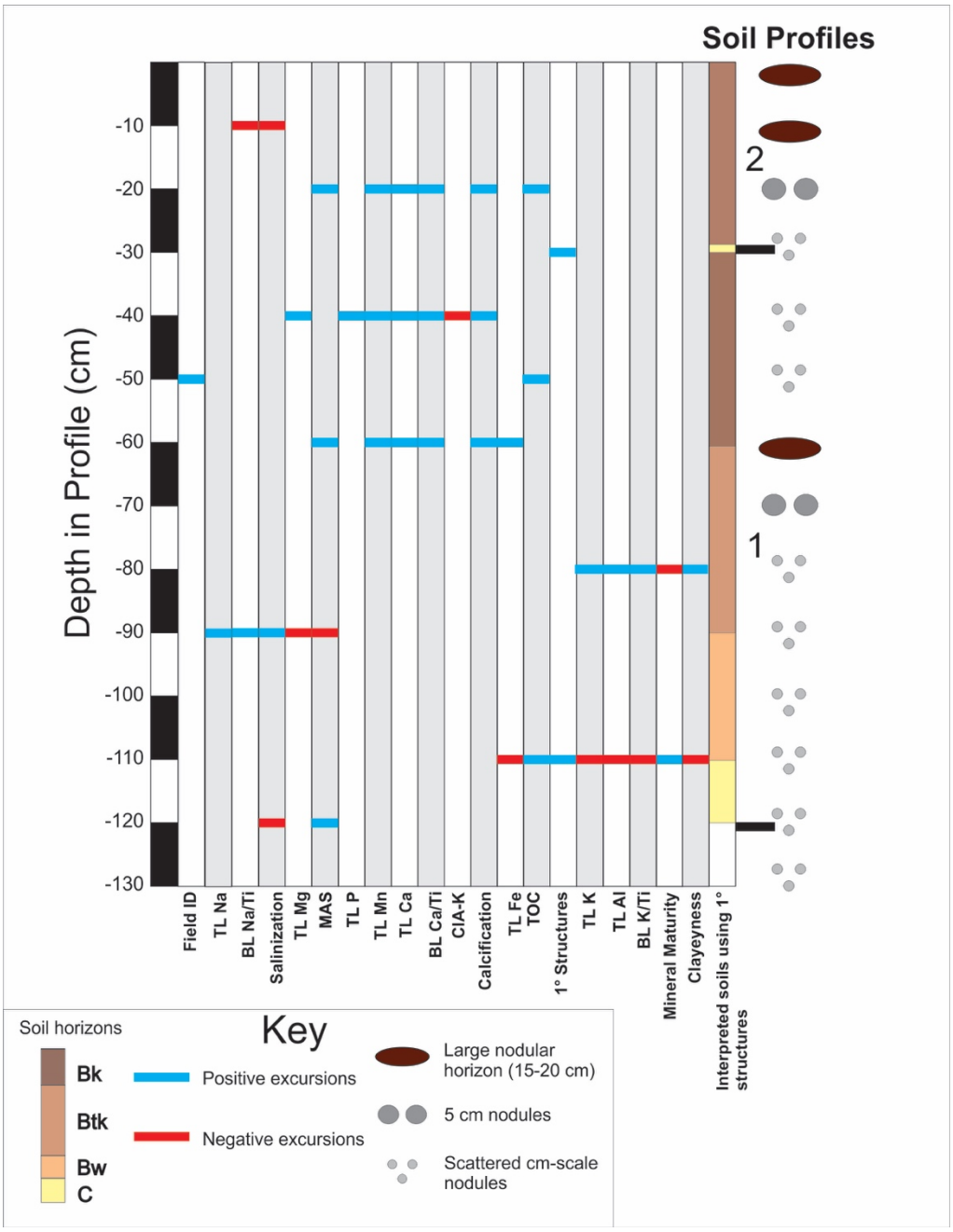

Figure 18. Graphic representation of where positive (blue) and negative (red) excursions occur in the various data sets. "TL" denotes elements plotted using mass balance calculations. "BL" denotes elemental ratios from the plot of base loss (Fig. 11A) and "MAS" is the mineral assemblage stability weathering proxy (Fig. 11E). Stacked soil profiles in the discussion is labeled adjacent to the soil-horizon interpretation.

TABLES

	wt%										
Sample	Na2O	Al2O3	K2O	CaO	MgO	MnO	SiO2	P2O5	TiO2	Fe2O3	ZrO2
280517.1	2.8	13.8	2.46	1.87	1.59	0.05	70.3	0.18	0.47	2.82	0.025
280517.2	2	14.55	3.23	2.69	1.88	0.08	65.5	0.14	0.54	4.37	0.021
280517.3	1.82	14.3	3.32	3.41	1.79	0.13	63.9	0.15	0.53	4.67	0.019
280517.4	1.88	14.5	3.37	2.36	1.68	0.07	64.6	0.12	0.54	4.73	0.019
280517.5	1.69	14.25	3.51	4.9	1.7	0.11	59.9	0.15	0.53	4.77	0.019
280517.6	1.81	14.85	3.66	2.83	1.7	0.09	64.2	0.13	0.55	4.86	0.021
280517.7	1.79	14.65	3.59	3.44	1.79	0.14	62.4	0.13	0.57	5.44	0.017
280517.8	2.07	15.4	3.82	1.73	1.64	0.06	65.9	0.11	0.55	4.86	0.021
280517.9	1.94	15.7	4.07	1.82	1.65	0.05	64.4	0.13	0.57	5.05	0.020
280517.1	2.62	14.9	3.38	1.91	1.33	0.04	67.4	0.1	0.53	3.99	0.027
280517.11	2.53	14.95	3.51	1.79	1.45	0.04	65.7	0.1	0.56	4.43	0.026
280517.12	2.77	14.5	2.96	1.26	1.36	0.05	69.4	0.11	0.58	4.1	0.023
280517.13	2.29	14.6	3.16	0.96	1.54	0.04	67.9	0.11	0.61	4.66	0.019
280517.14	2.48	15.7	3.59	1.23	1.57	0.04	66	0.12	0.61	5.04	0.023

Table 1. Major-element-oxide (including Ti and Zr) results from ICP-MS analysis conducted by ALS Laboratories, Las Vegas, NV (completed January 27, 2018). Molecular abundances are in wt.%.

Sample number	Depth (cm)	Siltstone color	Primary features in thin section	Comments
280517.1	0	5GY 4/1 dark greenish gray	Homogenous	
280517.2	10	5GY 4/1 dark greenish gray	N/A	
280517.3	20	5GY 4/1 dark greenish gray	N/A	
280517.4	30	5GY 4/1 dark greenish gray	Coarse-fine couplets	Single large mud clast
280517.5	40	5GY 4/1 dark greenish gray	Homogenous	Abundant mud chips
280517.6	50	5GY 4/1 dark greenish gray	Homogenous	Abundant mud chips
280517.7	60	5GY 4/1 to 5GY 2/1 dark greenish gray to dark black	Burrows	Abundant mud clasts
280517.8	70	5GY 4/1 dark greenish gray	Homogenous	Abundant mud chips
280517.9	80	5GY 4/1 dark greenish gray	N/A	
280517.10	90	5GY 4/1 dark greenish gray	Homogenous	Single large mud clast, visible cubic pyrite
280517.11	100	5GY 4/1 dark greenish gray	Homogenous	
280517.12	110	5Y 6/1 olive gray	Coarse-fine couplets, flame structures	Two large mud clasts, visible cubic pyrite
280517.13	120	5GY 4/1 dark greenish gray	Coarse-fine couplets, horizontal and sub vertical burrows	
280517.14	130	5GY 4/1 dark greenish gray	Homogenous	Sparse mud chips

Table 2. Characteristics of the fourteen samples collected from the calcic paleoVertisol interval. The color of the hand sample and collection depth are listed. Primary features seen in thin section—as well as other notable features—are also listed. "N/A" denotes samples for which thin sections were not available due to incompetent nature of the rock.

Sample Depth (cm)	Sample ID	Weight% CC	$\delta^{13}C$ (‰VPDB)	^{13}C Std Dev	$\delta^{18}O$ (‰VPDB)	^{18}O Std Dev
20	280517.3 nodule	25	-8.62	0.007	-21.24	0.007
20	Upper calcic paleosol	60	-5.58	0.005	-21.59	0.043
70	280517.8 nodule center	59	-8.08	0.013	-21.24	0.031
70	280517.8 nodule periphery	64	-5.49	0.009	-21.71	0.013
70	280517.8 nodule periphery R	62	-5.49	0.016	-21.67	0.004
70	Lower calcic paleosol	57	-5.44	0.021	-21.71	0.020

Table 3. Data table showing the weight% of calcium carbonate, $\delta^{13}C$ (‰VPDB), standard deviation of ^{13}C, $\delta^{18}O$ (‰VPDB), and the standard deviation of ^{18}O obtained from micritic calcite. Nodules obtained from a depth of 70 cm in the calcic paleoVertisol interval were analyzed at their centers and around their peripheries because of the septarian cracks. All data were collected at Neil Tabor's laboratory at Southern Methodist University in Dallas, Texas.

Horizon	Characteristics	Climatic/environmental significance
A	Mineral horizon of eluviation with highest amount of organic matter (unless O horizon is present)	Not always present in paleosols due to erosion of profile tops
B	Zone of illuviation and development of soil structure	
C	Weakly weathered zone with little soil structure	
Horizon modifiers		
t	Accumulation of phyllosilicates	Phyllosilicates accumulate typically in soil profiles that are well-drained, most often in environments that experience seasonal rainfall
w	Soil structure or color present, but little evidence of illuviation	Soil-forming conditions present.
k	Carbonate accumulation greater than that of the parent material	Carbonate salts typically accumulate in sub-humid to semi-arid environments were evaporation exceeds precipitation.

Table 4. Soil horizons and modifiers relevant to study. Adapted from Thomas et al. (2011).

		Molar Ratio		Climofunctions		
Sample	Depth (cm)	CIA-K	Salinization (K+Na)/Al	MAP (mm/yr)	MAT (° C)	Bt horizons based on CIA-K values
280517.1	0	63.3	0.53	768.83	7.56	
280517.2	10	64.0	0.47	779.88	8.67	x
280517.3	20	60.9	0.46	733.06	8.78	
280517.4	30	66.3	0.46	815.23	8.70	
280517.5	40	54.9	0.46	652.23	8.76	
280517.6	50	64.6	0.47	789.65	8.66	
280517.7	60	61.4	0.47	741.21	8.67	
280517.8	70	70.2	0.49	880.29	8.24	
280517.9	80	70.7	0.48	890.09	8.35	x
280517.10	90	65.7	0.53	806.11	7.41	
280517.11	100	66.8	0.53	824.62	7.45	
280517.12	110	67.9	0.54	842.39	7.40	
280517.13	120	72.6	0.49	923.53	8.19	
280517.14	130	71.3	0.51	900.54	7.91	

Table 5. CIA-K and MAP values calculated from ICP-MS molar wt. percent. Bt horizons based on positive CIA-K excursions occur at depths of 10 cm and 80 cm.

APPENDICES

Appendix 1

Six sandstone samples from above and below the paleosol interval were cut to standard thin-section slide size and were sent to Applied Petrographic Services in Greensburg, PA, from which thin sections were made. Grain size and provenance analyses of the six sandstone-thin sections are used to determine the sand-to-silt ratio as well as the proportion of quartz, feldspar, and lithic grains (QFL). The transect method was used to measure the maximum diameter of at least 300 grains in each thin section; each thin section was viewed with a Nikon Eclipse LV100 POL petrographic microscope under 10x/0.3 magnification. The microscope was connected to a Nikon DS-Ri1 camera and a computer running NIS-Elements BR 3.1 imaging software, which allowed for the field-of-view of the microscope at different magnifications to be updated on the computer in real-time. Grain-size measurements were made digitally using the length-measurement tool by selecting the two points farthest from each other on a single grain. The grains were categorized as either sand (>0.0625 mm) or silt (<0.0625 mm) based on their maximum diameter. After 300 grains were measured, the ratio of sand:silt was calculated. Any sample with a ratio greater than 1.0 was categorized as a silty-sandstone, and any sample with a ratio lower than 1.0 was categorized as a sandy-siltstone. These latter samples were discarded from further sandstone analysis.

All samples identified as silty-sandstone were analyzed for basic mineralogy (quartz, feldspar, or lithic) using the same petrographic microscope setup. A point count was performed digitally using NIS-Elements. To begin, the thin section was secured onto the stage, and the stage orientation was set to 0°. Next, an evenly-spaced 80 μm grid was overlaid onto a live digital-image of the thin section viewed under 10x/0.3 magnification. This allowed the thin section to be rotated

under the microscope with the computer updating the digital field-of-view image in real-time. The mineralogy of any sand-sized grain on which the cross-hairs of the grid landed (at stage orientation of 0°) was identified under cross-polarized light and recorded in Excel. If the stage was rotated to identify the mineralogy of a grain, it was reset back to 0° before identification of the next grain. At least 300 grid-points for each thin section were identified. QFL ternary diagrams for the silty-sandstone thin sections were made in Grapher.

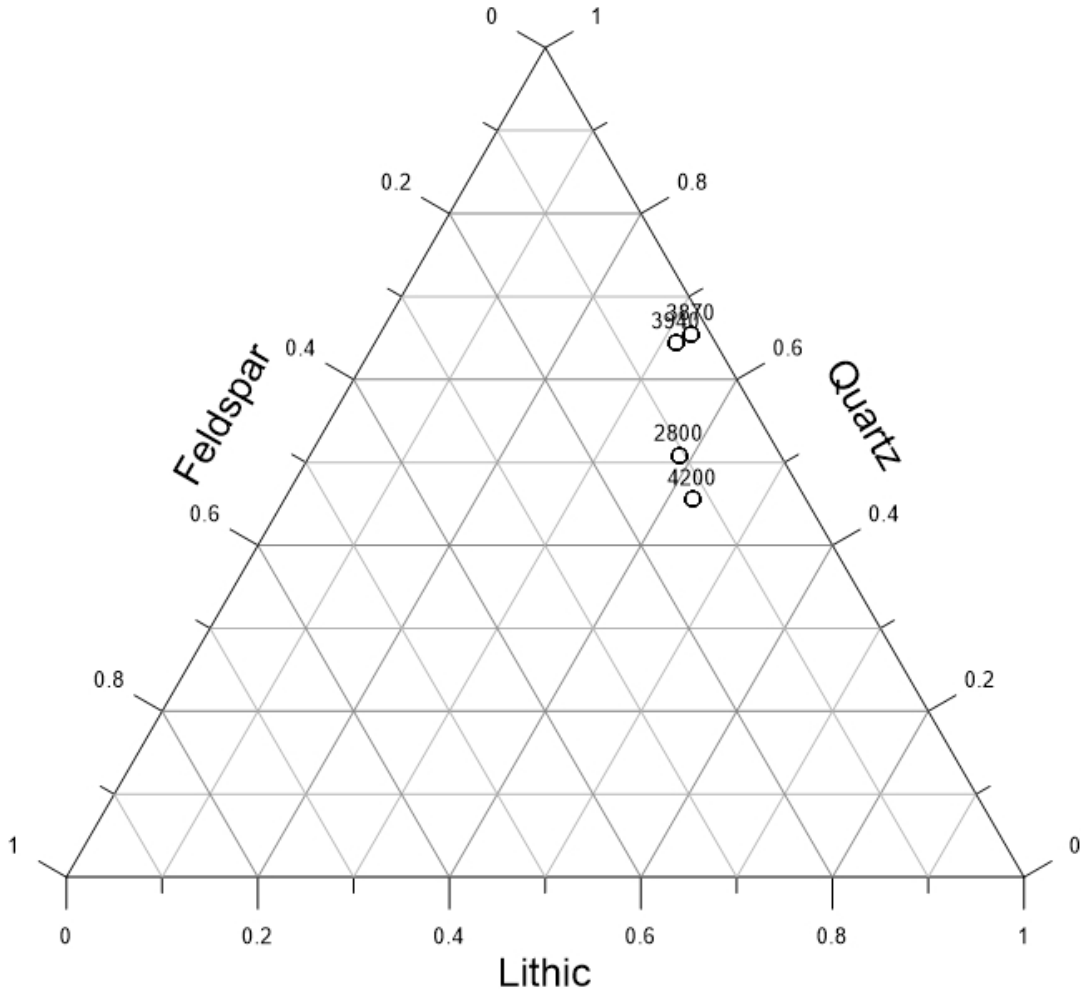

Appendix 1. Ternary diagram showing the proportion of quartz, feldspar, and lithic sand-sized grains in four silty sandstones taken from stratigraphic heights of 28 m, 38.7 m, 39.4 m, and 42 m. All sandstone samples plot as lithic wackes.

Appendix 2

Bulk-rock samples were ground flat on two sides and glued to standard glass petrographic microscope slides. All samples were run in the Brüker M4 Tornado X-ray fluorescence (XRF) instrument between 0.25 keV and 20.00 keV, with a live time of 30 s per sampling point (25 μm). Data were analyzed—with the Bruker analytic software—for the following elements: Si, Al, K, Fe, Na, Mg, Ca, Ti, Mn, P, S, and Zr. A grid of at least 50 sample points was randomly selected under 10x magnification on the upward-facing flat side of the bulk-rock sample.

	Wt%										
Sample	Na2O	Al2O3	K2O	CaO	MgO	MnO	SiO2	P2O5	TiO2	Fe2O3	ZrO2
280517.1	1.59	7.91	3.10	3.10	0.89	0.054	33.14	0.012	0.35	2.89	0.028
280517.2	1.37	8.09	3.53	3.53	0.97	0.068	32.22	0.000	0.35	3.65	0.030
280517.3	1.17	8.52	4.01	4.01	0.90	0.073	31.50	0.003	0.42	4.11	0.035
280517.4	1.46	7.72	3.51	3.51	0.84	0.072	32.58	0.007	0.41	3.91	0.026
280517.5	1.19	8.44	4.21	4.21	0.85	0.077	30.53	0.006	0.45	4.49	0.043
280517.6	1.34	8.22	3.81	3.81	0.76	0.087	30.99	0.032	0.41	4.18	0.031
280517.7	1.17	8.34	4.21	4.21	0.86	0.094	31.08	0.003	0.42	4.53	0.032
280517.8	1.09	5.77	2.89	2.89	0.75	0.53	22.34	0.059	0.30	2.93	0.030
280517.9	1.34	8.88	4.45	4.45	0.79	0.054	31.09	0.000	0.41	4.45	0.038
280517.1	1.99	8.06	3.39	3.39	0.64	0.035	33.18	0.002	0.33	3.25	0.084
280517.11	1.90	8.39	3.89	3.89	0.88	0.036	32.09	0.002	0.40	3.78	0.035
280517.12	2.05	8.14	3.41	3.41	0.71	0.034	32.67	0.000	0.44	3.72	0.028
280517.13	3.02	7.38	3.36	3.36	1.10	0.032	32.15	0.000	0.45	3.64	0.031
280517.14	1.91	8.42	3.94	3.94	0.71	0.035	31.93	0.018	0.42	3.98	0.028

Appendix 2. Major-element-oxide (including Ti and Zr) results from 50-point XRF analysis obtained using a Brüker M4 Tornado instrument.

Appendix 3

Bulk-rock samples were ground flat on two sides and glued to standard glass petrographic microscope slides. All samples were run in the Brüker M4 Tornado XRF between 0.25 keV and 20.00 keV, with a live time of 30 s per sampling point (25 μm). Data were analyzed—with the Bruker analytic software—for the following elements: Si, Al, K, Fe, Na, Mg, Ca, Ti, Mn, P, S, and Zr. A grid of at least 300 points selected under the same conditions was also sampled for six of the bulk-rock samples down the profile.

	Wt%										
Sample	Na2O	Al2O3	K2O	CaO	MgO	MnO	SiO2	P2O5	TiO2	Fe2O3	ZrO2
280517.1	1.68	7.75	3.27	1.96	0.88	0.06	32.84	0.02	0.41	3.01	0.03
280517.3	1.18	8.35	4.04	2.33	0.94	0.09	30.94	0.00	0.47	4.56	0.03
280517.5	1.47	7.95	3.83	1.80	0.86	0.10	31.75	0.00	0.43	4.39	0.04
280517.8	1.20	8.22	4.28	3.24	0.84	0.09	30.21	0.01	0.53	4.74	0.04
280517.11	1.22	8.68	4.83	1.05	0.80	0.05	30.99	0.01	0.47	4.84	0.03
280517.14	1.91	8.20	4.17	1.11	0.67	0.04	31.75	0.01	0.46	4.24	0.05

Appendix 3. Major-element-oxide (including Ti and Zr) results from 300 point XRF analysis obtained using a Brüker M4 Tornado instrument.

Appendix 4

Thin section samples were analyzed under a magnification of 100x for major-element compositions of the matrix between siliciclastic grains. A range of 100 to 150 sample points were individually selected to ensure that only the matrix was sampled. All samples were run in the Brüker M4 Tornado XRF between 0.25 keV and 20.00 keV, with a live time of 30 s per sampling point (25 μm). Data were analyzed—with the Bruker analytic software—for the following elements: Si, Al, K, Fe, Na, Mg, Ca, Ti, Mn, P, S, and Zr.

	Wt%									
Sample	Na2O	Al2O3	K2O	CaO	MgO	MnO	SiO2	P2O5	TiO2	Fe2O3
280517.1	2.26	7.43	2.53	1.93	0.70	0.04	34.49	0.01	0.32	1.20
280517.2	N/A	N/A	N/A	N/A	N/A	N/A	N/A	N/A	N/A	N/A
280517.3	N/A	N/A	N/A	N/A	N/A	N/A	N/A	N/A	N/A	N/A
280517.4	1.58	7.37	3.25	6.38	0.60	0.14	31.50	0.01	0.28	1.55
280517.5	3.90	0.35	3.90	5.51	5.51	0.08	0.08	1.89	0.35	1.89
280517.6	1.09	8.70	4.41	2.73	0.83	0.07	31.86	0.01	0.33	2.16
280517.7	0.97	5.64	2.64	9.48	0.63	0.15	31.72	0.00	0.24	1.63
280517.8	1.34	9.19	4.57	1.06	0.80	0.02	32.53	0.01	0.28	1.87
280517.9	N/A	N/A	N/A	N/A	N/A	N/A	N/A	N/A	N/A	N/A
280517.10	1.99	8.19	3.74	4.47	0.56	0.07	31.68	0.01	0.27	1.43
280517.11	1.35	7.17	3.74	15.54	0.57	0.17	25.62	0.01	0.28	1.51
280517.12	1.22	4.88	1.33	34.52	0.41	0.38	17.14	0.03	0.16	0.82
280517.13	1.87	8.17	3.61	0.94	0.62	0.02	33.83	0.00	0.34	1.85
280517.14	2.10	9.11	4.09	0.96	0.69	0.03	32.17	0.01	0.30	2.47

Appendix 4. Major-element-oxide (including Ti) results from 100-150 point XRF analysis using a Brüker M4 Tornado instrument. "N/A" denotes samples for which thin sections were not able to be made, and thus no matrix data was collected.

Appendix 5

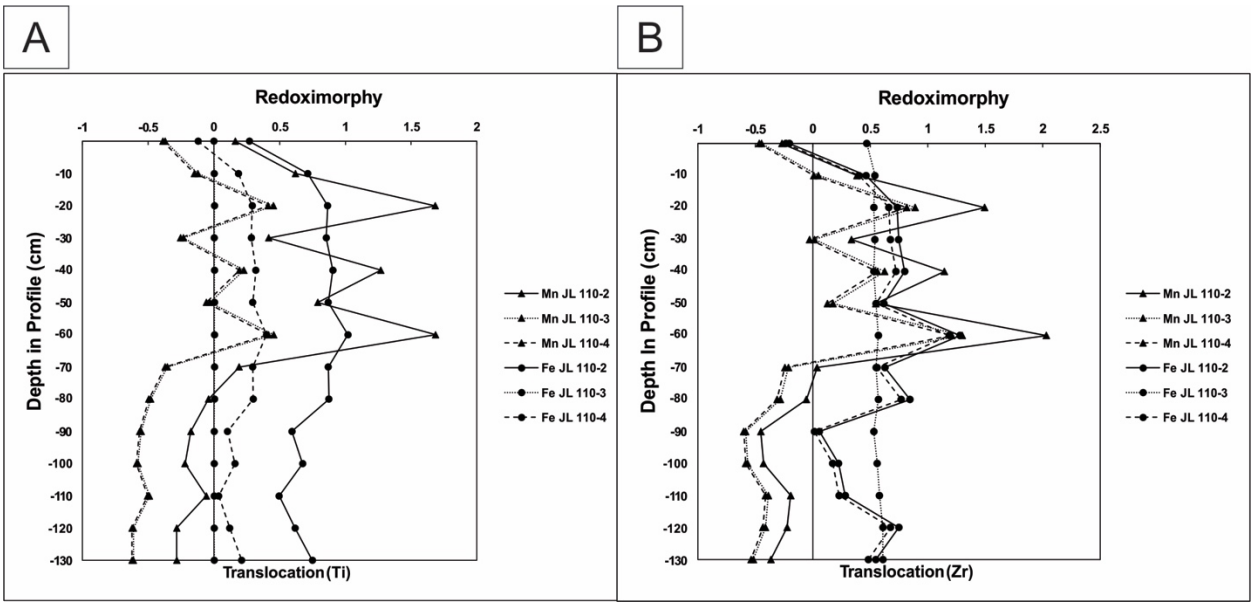

Appendix 5. Translocation of Mn and Fe in the 1.3-m calcic paleoVertisol profile. Data were compared against three different samples from Li et al. (2017) considered to represent parent materials. Although relative enrichment and/or depletion varies based on the parent material used, the overall trends are consistent. A. Trends plotted against depth in profile using Ti as immobile element. B. Trends plotted against depth in profile using Zr as immobile element.

Appendix 6

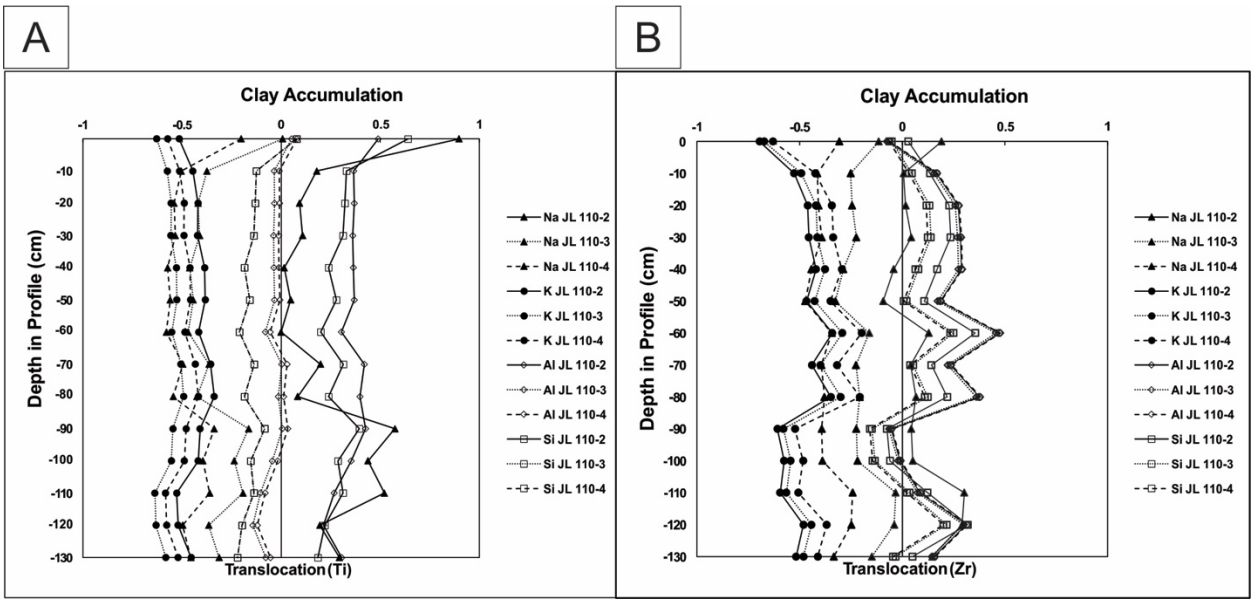

Appendix 6. Translocation of Na, K, Al, and Si in the 1.3-m calcic paleoVertisol profile. Data were compared against three different samples from Li et al. (2017) considered to represent parent materials. Although relative enrichment and/or depletion varies based on the parent material used, the overall trends are consistent. A. Trends plotted against depth in profile using Ti as immobile element. B. Trends plotted against depth in profile using Zr as immobile element.

Appendix 7

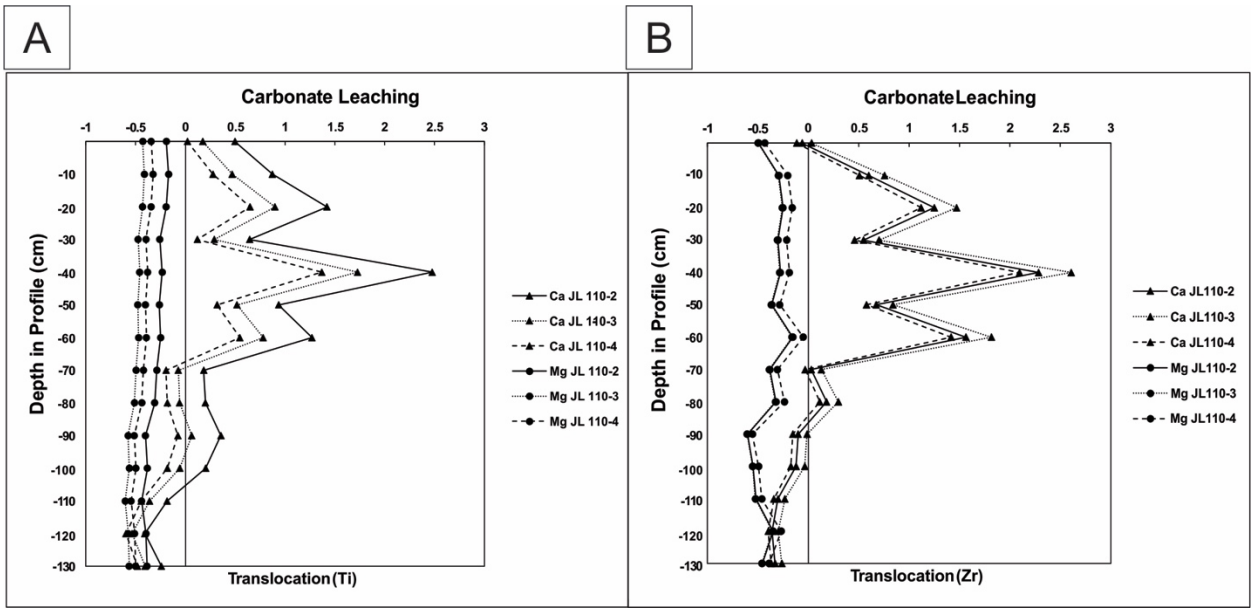

Appendix 7. Translocation of Ca and Mg in the 1.3-m calcic paleoVertisol profile. Data were compared against three different samples from Li et al. (2017) considered to represent parent materials. Although relative enrichment and/or depletion varies based on the parent material used, the overall trends are consistent. A. Trends plotted against depth in profile using Ti as immobile element. B. Trends plotted against depth in profile using Zr as immobile element.

Appendix 8

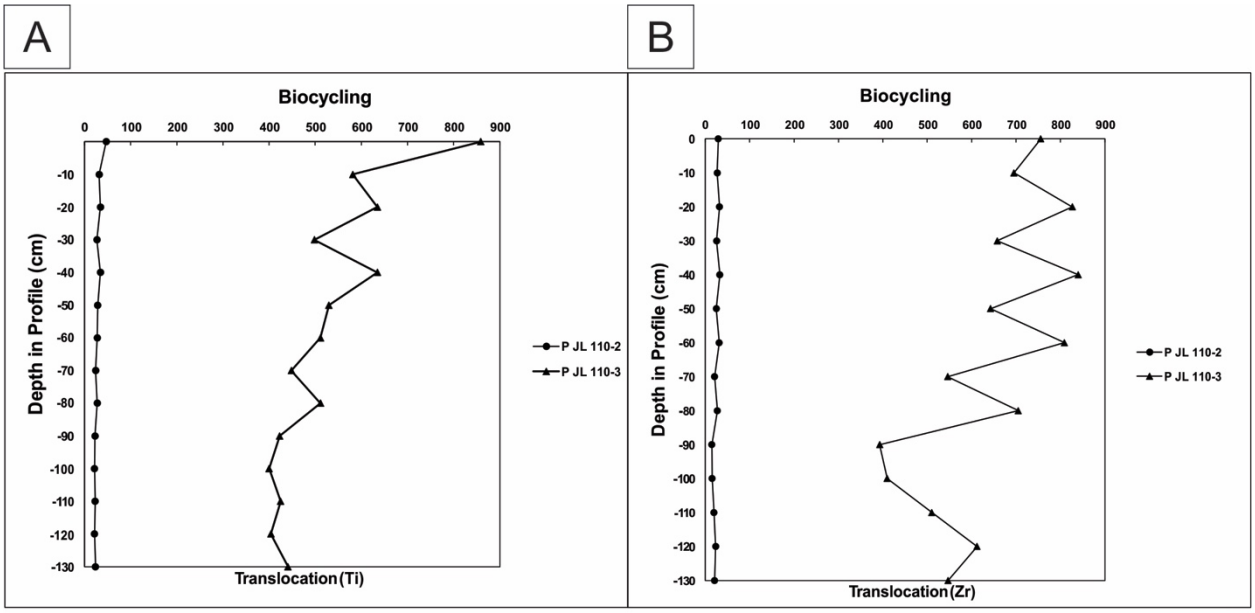

Appendix 8. Translocation of P in the 1.3-m calcic paleoVertisol profile. Data were compared against two different samples from Li et al. (2017) considered to represent parent materials. A biocycling plot using the parent material JL 110-4 was not generated due to insufficient wt% P in this sample against which to calculate translocation. Although relative enrichment and/or depletion varies based on the parent material used, the overall trends are consistent. A. Trends plotted against depth in profile using Ti as immobile element. B. Trends plotted against depth in profile using Zr as immobile element.

Appendix 9

All bulk-rock soil-profile samples were powdered with a mortar and pestle to measure percent total organic carbon (%TOC). Three %TOC values were measured for each sample using a Perkin Elmer 2400 Series II CHNS/O elemental analyze, and the averages were computed and graphed versus depth in profile using Excel. Percent TOC was measured against acetanilide standards (C = 71.09%, H = 6.71%, N = 10.36%, O = 11.84%), which were run every 10 samples, as unknowns, to ensure data integrity and reproducibility.

The percent total carbon loss on ignition (%LOI) was measured by ALS Global. To measure %LOI, a prepared sample (1.0 g) was placed in an oven at 1000° C for one hour, cooled, and then weighed. The %LOI was calculated from the difference in weight and does not discriminate between organic and carbonate forms of carbon. To calculate percent total inorganic carbon (TIC), TOC was subtracted from LOI values.

All %TOC values are <1%, with a minimum value of 0.24% at a depth of 10 cm and a maximum value of 0.87% at a depth of 50 cm (Appendix 9). There are two significant excursions in TOC at depths of 50 cm and 110 cm. Significant positive excursions in %TOC are determined by having values that are at least two times the standard error greater or lesser than the values directly stratigraphically above or below. There is a possible excursion in %TOC at a depth of 20 cm; even though there is a 0.003% TOC overlap with the error bar of the sample taken at a depth of 30 cm, the overlap in error is so small that the excursion at a depth of 20 cm is still presented as statistically significant. These three excursions represent the tops of negative trends that continue down the profile (Appendix 9).

Percent LOI and %TIC follow the same trends down the profile. TIC was calculated by subtracting %TOC from %LOI. LOI values range from 3.07% at a depth of 0 cm to 6.28% at a

depth of 40 cm (Appendix 9). LOI has a positive trend from a depth of 0 cm to 40 cm, followed by a negative trend from a depth of 40 cm to 1.3 m.

Considerations for soil-profile interpretation. --- The two data sets that are probably the strongest indicators of soil boundaries are %TOC and the physical characteristics (primary sedimentary structures) as observed in the thin sections. These data combined, however, do not support the consistent demarcation of stacked soil profiles. Positive excursions of %TOC occur at depths of 20 cm, 50 cm, and 110 cm (Fig. 18), and %TOC is expected to be concentrated at the tops of soil profiles. This is because organic matter, such as leaf-and-stem litter, accumulates at the air:soil interface in the O-horizon and is translocated down to the A-horizon. Here, the peaks in %TOC are interpreted to be A-horizons because there are no beds of preserved organic material—such as those described by Gastaldo et al. (2014) at Wapadsberg Pass—in the Quaggasfontein section. In contrast, well preserved primary structures are expected to be found at the *base* of soil profiles due to the less-weathered and pedogenically altered fabrics. The co-occurrence of primary structures at or directly beneath the positive %TOC excursions at depths of 20 cm and 110 cm is confounding.

A possible explanation for why an A-horizon might occur at (or directly above) the same depth at which primary structures are unaltered is that the peak %TOC horizon actually may represent reworked A-horizons that have been introduced into the floodplain. The introduction of reworked A-horizon material would have been followed by deposition of new "parent" sediment, thereby burying the reworked organics and protecting them from subsequent pedogenic modification but not from decay. This may be evidenced by reworked soil aggregates or fragmented peds, which are seen in thin sections 280517.4 (Fig. 7B), 280517.7 (Fig. 9A), 280517.10 (Fig. 9C), and 280517.12 (Fig. 8A). These thin sections correspond with depths of 30

cm, 60 cm, 90 cm, and 110 cm, respectively. The presence of these aggregates at the same/similar depths to high %TOC values at depths of 20 cm, 50 cm, and 110 cm supports the interpretation that reworked soils may have been deposited along with fresh parent material prior to the formation of new soils. Presented below is an alternative soil-profile interpretation made under the assumption that the primary structures represent the true basal soil boundaries and that the high %TOC values do not represent original A-horizons.

TOC Profile 1: 110 cm to 130 cm. --- Only 20 cm of the lowermost soil profile were sampled, leaving few data on which to interpret the soil-forming conditions. A negative excursion in salinization and a positive excursion in MAS occur at a depth of 120 cm (Fig. 18). Their relative proximity to the top of the inferred soil profile may imply dry soil conditions, which preserved the translocation of salts or the weathering of original minerals. However, because this is only a partial soil profile, no conclusive interpretation can be made. Due to the presence of abundant cm-scale calcium-carbonate-cemented nodules from a depth of 110 cm to 130 cm, this interval is defined as a Bk-horizon.

TOC Profile 2: 50 cm to 110 cm. --- This interval exhibits positive excursions at depths of 60 cm, 80 cm, and 90 cm. The excursion at a depth of 60 cm is interpreted as a result of the translocation of leachable elements when water was available. Ca, as well as total carbon (both organic and inorganic; Appendix 19), is concentrated in the matrix at this depth. The positive covariance of Ca and C implies that perhaps less calcium carbonate is sequestered in nodules at this depth. Additionally, the high abundance of Mn at a shallower depth is suggestive of low soil moisture (Driese et al., 2000; Stiles et al., 2003). The interpretation of low soil moisture, however, is not supported by Mg, Na, K, and Al trends that show excursions at depths of 80 and 90 cm. Mg, Na, and K are commonly leached or biocycled elements (Stiles et al., 2003), and Al accumulates

in clay minerals (Sheldon and Tabor, 2009). These elements, therefore, are expected to be concentrated at lower depths when moisture levels are adequate to allow for translocation through the soil. These contradictory interpretations may be reconcilable if pedogenic overprinting is considered as a factor.

Pedogenic overprinting occurs when soils experience several changes in soil-forming conditions over time, and these changes can affect the geochemical signature of the soil. These soils are called polygenetic. The excursion at a depth of 60 cm—which is indicative of low soil moisture—might be the result of overprinting from a period when this soil experienced greater evaporation and less precipitation. The excursions at depths of 80 cm and 90 cm, then, may be more indicative of the soil moisture regime when the second profile was first forming, whereas the excursions at a depth of 60 cm may be indicative of later, dryer conditions that overprinted the second soil profile. Based on the presence of carbonate-forming minerals at a depth of 60 cm, this has been interpreted as a Bk-horizon, which is underlain by a Btk-horizon from a depth of 60 cm to 90 cm. A Bw-horizon is interpreted from a depth of 90 cm to 110 cm based on the depletion of major elements such as Fe, K, and Al at the base of this interval (Fig. 18).

TOC Profile 3: 20 cm to 50 cm. --- The prominent excursions in this soil profile occur at depths of 20 and 40 cm. Data resolution and continuity are too poor to determine if there are, truly, increasing downward trends approaching each peak value, as these are only separated by a single data point. Therefore, based on the data available, the excursions at depths of 20 cm and 40 cm are considered to be a zone of elevated values. If this "zone" of elevated values is expanded to include positive excursions in similar elements that also occur at a depth of 60 cm, then the interpretation of pedogenic overprinting applies to the third soil profile as well as the second. This profile appears to have been overprinted with a low moisture signature that also affected the second soil profile

below. The high accumulation of carbonate-forming elements in this soil profile supports the interpretation of a Bk-horizon that spans the profile.

TOC Profile 4: 0 cm to 20 cm. --- There are negative excursions for base loss (Na/Ti) and salinization at a depth of 10 cm (Fig. 18). Because no data exists above a depth of 0 cm due to the presence of an overlying sandstone body (Fig. 2), it is likely that this 20-cm profile is incomplete and represents just the lower horizon(s) of a soil. The negative excursions in base loss and salinization at a depth of 10 cm are indicative of low moisture when the soil was forming (Driese et al., 2005). Salts are likely to accumulate at lower depths in a soil when the MAP is high. Hence, low values near the base of the soil profile indicate relatively low MAP (Driese et al., 2005). This 20-cm profile is interpreted to represent a Bk-horizon based on both the large nodular horizons present at depths of 0 cm and 10 cm and the 5-cm-diameter nodules at a depth of 20 cm.

Comparison of soil profile interpretations. --- Four stacked soil profiles are identified when %TOC is used as the defining criterion to identify soil boundaries, and only two stacked soil profiles are identified when primary structures are used to define them (Fig. 18). The distribution of soil horizons in the 1.3-m interval is not altogether very different for each set of soil interpretations. However, because of the possibility that the high %TOC values are a result of reworked A-horizons and are not indicative of an original A-horizon, the soil-profile interpretations based on primary structures may be a more reliable interpretation.

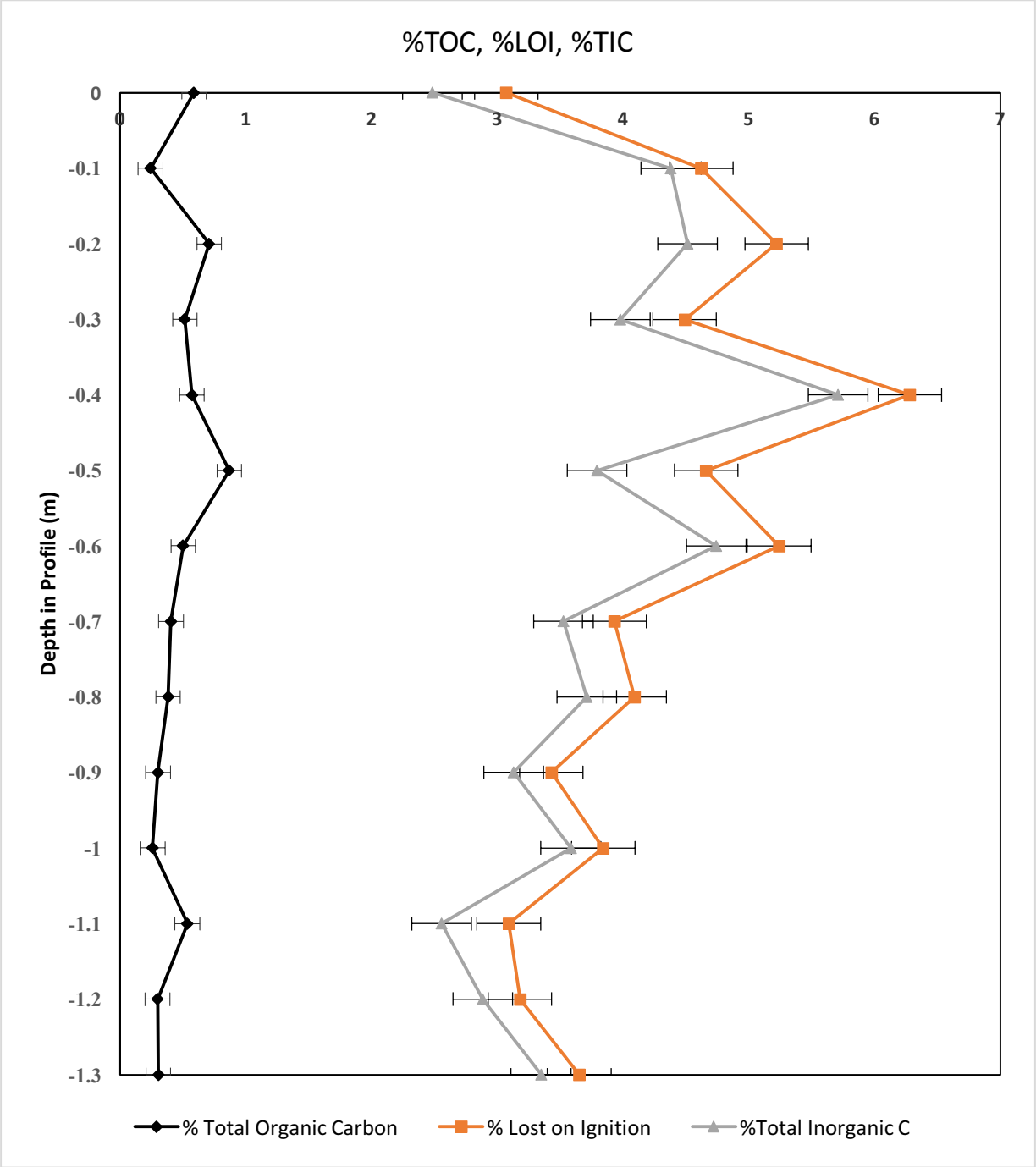

Appendix 9. Graphs of % total organic carbon (TOC; black), % carbon loss on ignition (LOI; orange), and % total inorganic carbon (TIC; gray), each plotted against sample depth in profile along with standard error bars for %LOI and %TIC, and two-times standard error bars for %TOC.

Appendix 10

When preforming mass-balance calculations on lithified paleosols, the unweathered regolith beneath the paleosols is typically sampled to be used as parent material. However, there was no well-defined C-horizon or regolith readily apparent in the field beneath the calcic paleoVertisol interval at Wapadsberg Pass. Therefore, this study initially used three samples (JL110-2, JL110-3, and JL110-46) taken from Li et al.'s (2017) study at Old Lootsberg pass—collected ~28 m above Smith and Botha-Brink's (2014) vertebrate defined PTB—as representative parent material for mass balance calculations. Each of Li et al.'s (2017) samples represents sediment interpreted as having been deposited as part of a channel-fill deposit and, hence, represents provenance. These samples had been previously prepared on glass thin sections from the clay-sized fraction of greenish-gray siltstone and new XRF elemental composition data were obtained. Mass balance graphs shown in Appendices 5-8 were produced using these three parent material samples for calculations.

There are three causes for concern with the use of the Li et al.'s (2017) data for mass-balance calculations: (1) the sediment was taken from the *Lystrosaurus* Assemblage Zone, which is positioned stratigraphically higher than the *Dicynodon* (*Daptocephalus*) Zone; (2) only the clay fraction was analyzed—using the Brüker M4 Tornado—so the data are perhaps not as representative as those produced by ICP-MS performed at ALS laboratory that include the silt fraction; and (3) the weathering rates in the *Lystrosaurus* Assemblage Zone may have been different than those in the *Dicynodon* (*Daptocephalus*) Assemblage Zone.

	Wt%										
Sample	Na2O	Al2O3	K2O	CaO	MgO	MnO	SiO2	P2O5	TiO2	Fe2O3	ZrO2
JL110-2	1.05	10.81	5.46	0.80	0.91	0.03	29.47	0.01	0.43	4.06	0.018
JL110-3	1.34	10.42	4.85	0.70	0.87	0.04	30.50	0.00	0.29	3.51	0.017
JL110-4	1.70	10.17	4.23	0.80	0.76	0.04	30.57	0.00	0.29	3.99	0.017

Appendix 10. Major-element-oxide (including Ti and Zr) results from Li et al. (2017).